Mon. Not. R. Astron. Soc. **319**, 393–413 (2000)

N-body model for M51 – II. Inner structure

Heikki Salo★ and Eija Laurikainen

Division of Astronomy, Department of Physical Sciences, University of Oulu, PO Box 3000, FIN-90014 Oulun yliopisto, Finland

Accepted 2000 April 4. Received 2000 March 27; in original form 1999 October 6

ABSTRACT

The spiral structure of M51 (NGC 5194) is studied by 3D *N*-body simulations utilizing 4×10^6 particles, with main interest in the stellar spirals observed in near-IR within 30 arcsec of the centre of M51. A multiple-encounter tidal model for the interaction with the nearby companion (NGC 5195) is studied, capable of accounting for the main spiral structure of M51, including the morphology and kinematics of the extended H I tail. Our model of M51 consists of a self-gravitating exponential stellar disc, embedded in an analytical bulge + halo potential ($M_{\rm disc}/M_{\rm tot} = 0.333$–$0.5$), producing the observed rotation curve with the steep rise within 15–20 arcsec. When evolved in isolation, this model is stable against large-scale bar instabilities, but develops recurrent inner $m = 2$ spiral structures inside about 50 arcsec, although these lack continuity with the weaker outer multiarm structures. The pattern speeds of the inner spirals exceed the $\Omega - \kappa/2$ maximum, thus lacking inner Lindblad resonance (ILR). For larger disc masses, the inner spirals tend to have an oval component. These inner spirals/ovals often show a temporary leading appearance, as a result of the reflection of wave packets from the centre. The azimuthal propagation of wave packets deviates from that of Lin–Shu waves, as they do not maintain constant pattern speeds, except near the centre. Also, the shape of spirals deviates from Lin–Shu waves, the radial distance between adjacent arms adjusting close to Toomre's critical wavelength.

We show that the *in situ* swing amplification of the tidally induced kinematic disturbances during the highly inclined passage of the companion is limited beyond about 100 arcsec. This is a result of the low frequency of external forcing, placing the ILR of the outer disc disturbances to about this distance. However, these disturbances initiate higher frequency tidal waves which propagate inward with the group velocity. The azimuthal propagation speeds increase during the inward propagation, enabling the tidal waves to pass over the $\Omega - \kappa/2$ maximum, and reach within 30 arcsec, after about 500 Myr of initial perturbation. The interference between separate tidal waves leads to amplitude variations along spiral arms resembling the observed variations. Inside 30 arcsec, the tidal wave joins in many instances rather smoothly with the pre-existing central arms, giving a continuous structure much like the observed one. Simulations with different inner slopes of the rotation curve indicate that a steep rise in the rotation curve of M51 is essential for the formation of the tightly wound inner spiral arms.

Key words: galaxies: individual: M51 – galaxies: interactions – galaxies: kinematics and dynamics – galaxies: spiral – galaxies: structure.

1 INTRODUCTION

M51 (NGC 5194) is a nearby, exceptionally well-studied grand-design spiral galaxy, the regular two-armed spiral structure of which extends in optical images from about 30 to 300 arcsec, winding 1.5 full revolutions. The visible disc is surrounded by an extended H I tail (Rots et al. 1990), reaching to a distance of $\simeq$15 arcmin. The most exciting recent observation (Zaritsky, Rix & Rieke 1993) has been the discovery of a pair of tightly wound stellar spirals inside 30 arcsec, tracing additional 1.5 revolutions around a central bar/oval at $r \approx 15$ arcsec. Although the amplitude of these innermost arms is quite weak (they can only be discerned in near-IR, after subtraction of the overall disc luminosity profile), and their pitch angle is smaller than that of the main spirals, they

★ E-mail: heikki.salo@oulu.fi

seem to form a smooth continuation of the main spiral structure. Inner spirals have recently been observed in some other galaxies (e.g. M100; Knapen et al. 1995), but none of these other cases shows similar continuity over such a large scale of distances. Consequently, the origin of the spiral structure of M51 has received a lot of theoretical interest.

The widely accepted explanation for the spiral structure in grand-design galaxies in general is the Lin–Shu hypothesis (Lin & Shu 1964), according to which the observed spirals represent quasi-stationary, rigidly rotating density wave patterns. The basic ingredient is the self-gravity of the spirals, which forces the pattern speed of density enhancements into a constant value over a range of radii. In linear treatment this is possible for $r_{\rm ILR} < r < r_{\rm OLR}$, where ILR and OLR refer to the inner and outer Lindblad resonance of the pattern, respectively. At these distances the frequency at which an individual particle encounters the crests of the m-fold spiral potential, $\pm m(\Omega - \Omega_{\rm p})$, equals the particle's epicyclic frequency κ (Ω denotes the angular speed of the particle, while + and − signs refer to ILR and OLR). During recent years the original treatment has evolved into a so-called modal approach (Bertin et al. 1977; see Bertin & Lin 1996): the spiral patterns are viewed as a superposition of a few basic inward and outward propagating modes, which are selected by the amplification processes and the boundary conditions in the inner and outer parts of the galactic disc, with the cool gas component playing an important role. This view of spirals as standing density waves overcomes the problem with the original hypothesis, namely the expected rapid radial propagation of amplitude associated with single wave packets (Toomre 1969). The existence of amplitude variations along spiral arms, for example as observed for M81, has been interpreted to support the modal theory (Lowe et al. 1994), as such variations would naturally arise from the superposition of modes. In the modal approach, the modes are assumed to have an intrinsic origin, in terms of mild instabilitites of galactic discs, whereas external perturbations have only a secondary role at most, for example by exciting transient rapidly decaying waves.

During recent years, the assumption of a quasi-stationary spiral structure has been questioned, most notably by Sellwood and his co-workers (e.g. Sellwood & Lin 1989; Sellwood & Kahn 1991). They have demonstrated that a local deficiency in the angular momentum distribution (a 'groove') can lead to a strong dynamical instability, which after reaching a sufficiently large amplitude may through resonance scattering initiate new instabilities of the same kind. As shown by Sellwood and co-workers, these instabilites can be so strong that they may well overshadow the much milder instabilites invoked by the modal theory.

In any case, the Lin–Shu theory has been applied to several grand-design galaxies, with M51 as one of the prime targets. In the M51 density wave fits, a single pattern speed has been assumed, with $\Omega_{\rm p}$ chosen in a manner that places ILR at the inner terminus of optical arms at $r \approx 30$ arcsec. The shape of the spirals is then obtained from the Lin–Shu dispersion relation, connecting the radial wave number to the pattern speed of the wave and the local properties of the disc. Quite acceptable fits have been obtained for $30 < r < 150$ arcsec (Tully 1974b; Shu, Stachnik & Yost 1971). Note that also in the context of the modal approach, the single wave fit should yield a good approximation for the basic modes (Bertin & Lin 1996). However, the above-mentioned tightly wound inner stellar spirals pose problems to these density wave fits. To extend the fit inside 30 arcsec, a considerably larger $\Omega_{\rm p}$ would be required, bringing the corotation radius [$\Omega_{\rm p} = \Omega(r_{\rm cr})$] uncomfortably close to the centre, making it difficult to match the outer structure (Tully 1974b). A possible solution would be the simultaneous existence of two quite different intrinsic modes: however, the observed (Zaritsky et al. 1993) smooth continuation of the spirals would then need an explanation.

The existence of the close prominent companion (NGC 5195) rises a question as to whether the spiral structure of M51, at least as seen in the present epoch, could be largely of tidal origin. Already the classical test particle simulations by Toomre & Toomre (1972) have demonstrated that a highly inclined nearly parabolic passage of the companion, with mass ratio ≈0.5, can reproduce the bridge and tail arm morphology, even if the close passage occurred only about 100–200 Myr ago. With the inclusion of the self-gravity of the disc (Zang 1976; Hernquist 1990), and by allowing longer duration for the perturbation (about 500 Myr), the simulations reproduce also the main spiral structure beyond about 50 arcsec. The extended tail is also formed naturally in prolonged interaction. It is thus quite evident that the present structure of M51 is strongly affected by interaction. Interesting open questions are whether tidal models could also reproduce the innermost spirals inside 30 arcsec, or even the central oval. Also, even if the origin of the innermost spirals were intrinsic, it would be important to address the interplay between possible pre-existing intrinsic spiral modes and transient external excitation. As remarked by Lin & Bertin (1995), it is crucial to investigate whether the observed amplitude variations in the spiral arms could be accounted for by tidal models.

We have recently proposed an N-body model for M51 (Salo & Laurikainen 2000, hereafter Paper I), in which the companion moves in a bound low-eccentricity orbit. This model, implying two disc-plane crossings within the last 500 Myr, accounts for many of the characteristics of M51, including the apparently counter-rotating kinematics of the extended H I tail (Rots et al. 1990), not reproduced by nearly parabolic, single passage models. In Paper I this *current* bound orbital configuration was attributed to the shrinking of a primordial much larger orbit via dynamical friction. However, because of a small number of simulation particles ($N \sim 10^5$), no attempt was made to follow the innermost regions.

The requirements for an attempt to simulate a complete M51-type structure are very stringent because of the large range of distances involved (several hundreds of arcsec for the extended tail, a few arcsec for the inner spirals and oval). Good gravity resolution is required throughout the system, which is possible only with a very large number of simulation particles. Also, the stability properties of the initial galaxy model must be realistic, implying that the rotation curve, random velocity distribution, and the distribution of the active disc mass must be carefully chosen. The perturbation must also be chosen so that it reproduces the main observational characteristics of the system. In what follows we choose a simple description for M51, in terms of an exponential stellar disc embedded in a rigid halo + bulge potential, producing a combined rotation curve close to the observed one. The influence of the gas component is neglected. Before applying the perturbation, we investigate the stability of the model in isolation, the importance of which has been stressed by Lin & Bertin (1995). The effects of various simulation-method related parameters (gravity softening, grid resolution, number of particles) are also checked. However, to keep the problem computationally manageable, we limit our attention to the last ∼600 Myr of the perturbation history.

In Paper I we showed that the tidal perturbation can overwhelm, at least temporarily, the possible pre-existing outer spiral

structures. In the current study we address the intrinsic/external origin of the innermost spiral structure of M51 within ≈30 arcsec, in terms of *N*-body simulations involving up to 4×10^6 self-gravitating particles and improved gravity resolution. We concentrate on the bound-encounter model of Paper I, although the behaviour of the tidal perturbation in the inner regions is shown to be insensitive to the details of the perturbation geometry. In Section 2 we describe our simulation method and initial models, while in Section 3 we analyse and compare in more detail the behaviour of the simulation disc with and without external perturbation. In Section 4 we discuss our results and in Section 5 present our conclusions.

2 SIMULATION METHOD AND MODELS

The simulations of the present study are carried out with a 3D multigrid code (Salo & Laurikainen 1993; see Salo 1991 for a detailed description of the 2D version), which uses comoving spherical-polar grids with exponential radial grid spacing for the evaluation of the gravitational potential. The main advantage of a grid-based algorithm is its ability to handle a large number of particles with modest CPU-time consumption; also, because of the polar nature of the grid, the best gravity resolution is achieved near the centre of the system. In the present study only the disc is self-gravitating, while the spherical component is described with an analytical force model. Compared to totally self-consistent disc + bulge + halo simulations (Hernquist 1990; Paper I), the use of an analytical halo + bulge makes it easier to vary the simulation parameters (rotation curve, for example) in a systematic manner, and also reduces considerably the CPU-time consumption. However, we also carried out a single experiment with a live bulge. The code allows both members of an interacting galaxy pair to be simultaneously studied with comoving grids (as in Paper I), since as a result of their exponential nature the grids can overlap in a large calculation region, and thus the forces from both systems can be evaluated at each particle location. However, in the current study we concentrate on the inner structure of the main disc and thus the disc of the companion is not included.

Here we report experiments with encounter geometries similar to those used in Paper I but with improved gravity resolution (softening is reduced by a factor of 16) and a vastly increased number of particles (by a factor of 20). This is essential for resolving the innermost portions of the disc. In most of the initial experiments $N_r \times N_\phi \times N_z = 64 \times 48 \times 25$ potential grids were employed, where N_r, N_ϕ, and N_z denote the number of divisions in radial, azimuthal and latitudinal directions, respectively. Radially the grid extends from 0.4 to 1800 arcsec, so in practice all particles stay within the grid (forces on the few particles occasionally falling on the central hole of the grid are evaluated by direct summation). The cell size, $\Delta r \approx r\Delta\phi \approx 2\pi r/N_\phi$, so that for example at $r = 15$ arcsec we have $\Delta r \approx 2$ arcsec. Typically $N = 4 \times 10^6$ particles are simulated: the number of particles within $r = 30$ arcsec is about 160 000, comparable to the *total N* in Paper I or in other M51 models. We also repeated the most important runs with a $144 \times 108 \times 25$ grid, having a resolution $\Delta r \approx 0.9$ arcsec at $r = 15$ arcsec.

The disc component of M51 is described with a self-gravitating exponential stellar disc, while for the combined inert halo + bulge potential an isothermal sphere is employed, with a smooth transition to a constant core density. Both the disc and halo are truncated at $r = 400$ arcsec. Our standard values are

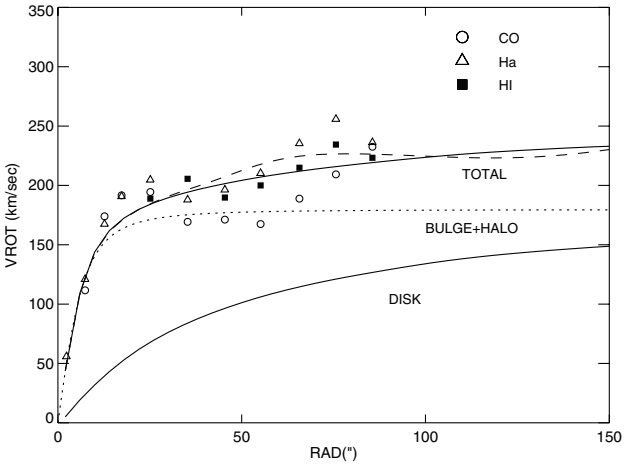

Figure 1. Inner rotation curve in the $M_d = 0.333$ model. Solid line shows the total circular velocity curve, while dotted and dash-dotted lines show separately the contributions from the bulge+halo and the disc, respectively. The disc curve is based on the azimuthally averaged radial force after ≈1 Gyr isolated evolution. Dashed line denotes the circular velocity curve in the perturbed model (450 Myr after the initial perturbation). Symbols denote various observations, redrawn from Rand et al. (1993).

$M_d = M_{disc}/M_{tot} = 0.333$, the exponential scalelength $R_e = 100$ arcsec and the halo core radius $R_c = 8$ arcsec. For $M_d = 0.333$, the disc contributes about 20 and 43 per cent of the total radial force for $r = 40$ and $r = 200$ arcsec, respectively. The companion is described with an isothermal halo ($R_c = 40$ arcsec, truncation at $r = 240$ arcsec), with relative mass $M_p = 0.55$ as compared to the primary galaxy. We assume the distance of 9.6 Mpc for M51, so that 400 arcsec corresponds to 18.6 kpc.

The inital velocities for disc particles are created with the epicyclic approximation, taking into account the correction for asymmetric drift (Binney & Tremaine 1987). The radial velocity dispersion is specified in terms of the Toomre parameter,

$$Q = \frac{\sigma_r \kappa}{3.36 G \Sigma}, \tag{1}$$

where σ_r is the radial velocity dispersion, G the gravitational constant, and Σ the disc surface density. The ratio of radial and tangential velocity dispersions, σ_r/σ_t, equals $2\Omega/\kappa$, while $\sigma_z/\sigma_r = 0.7$, where σ_z denotes the vertical velocity dispersion. The vertical profile obeys the isothermal sheet model (Spitzer 1942). The value $Q = 1.5$ is adopted unless otherwise indicated. The rotation curve of our M51 model (Fig. 1) matches the observed (Tully 1974a; Tilanus & Allen 1991; Rand 1993) steep rise within $r < 15$–20 arcsec, followed by a more or less flat portion. Orbital integrations are carried out with the standard time-centred leapfrog. The time step is chosen in the manner that guaranties at least 30 steps/rotation even in the central parts; for most of the disc the rotation period equals several hundreds of steps. Formally, the number of steps should always exceed the number of azimuthal bins: however, because of explicit gravity softening, the grid actually oversamples the potential in the innermost regions, which thus does not deviate significantly between adjacent bins. This was checked by repeating the most important runs with a two-times-shorter time-step, without any noticable difference. The orbital period at $r = 200$ arcsec equals about 250 Myr, while in the rising inner portion of the rotation curve the orbital periods are ≈15–30 Myr. The number of steps in

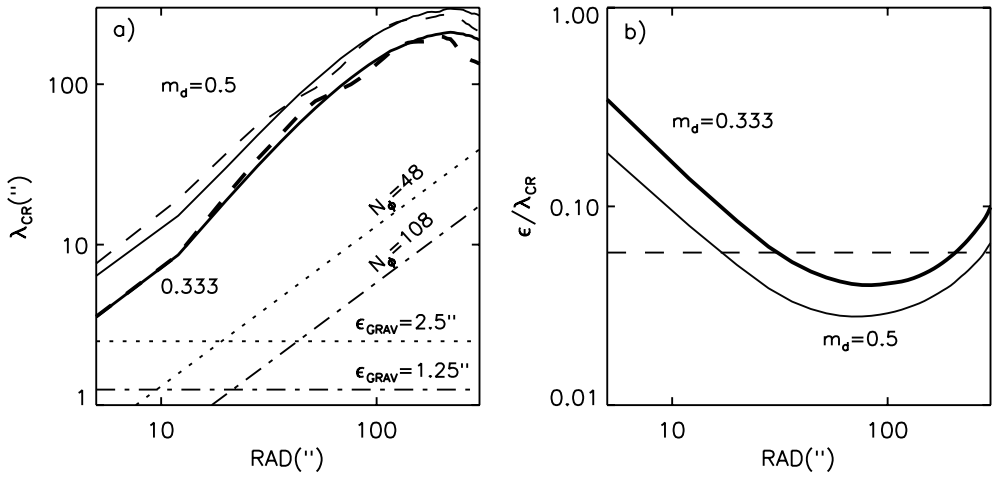

Figure 2. In (a) the critical wavelength $\lambda_{\rm cr}$ in simulations is displayed: thick and thin lines are the initial curves for $M_{\rm d} = 0.333$ and 0.5, respectively, while dashed lines correspond to the modifed values after perturbation. Also shown are the explicit and grid softening in simulations with the coarse resolution (N_ϕ, $\epsilon_{\rm grav} = 48$, 2.5 arcsec; dotted lines) and improved resolution (108, 1.25 arcsec; dash-dotted lines). In (b) the ratio $\epsilon/\lambda_{\rm cr}$ is shown for runs with improved resolution. The dashed vertical line corresponds to $\epsilon_{\rm cr} = \lambda_{\rm cr}/(2\pi e)$.

the longest runs was 16 000, requiring about ten days of CPU time on the Sun Ultra Enterprise 4000 server.

Before starting the perturbation, the disc is always evolved in isolation (for $\approx$1 Gyr) to allow the phase space distribution to relax. This is important as the epicyclic approximation is not accurate when the random velocities are not small compared to the circular velocity. This causes a slight initial redistribution of mass, seen as transient $m = 0$ undulations, which fade away in about 0.5 Gyr. Also, the initial truncation of the disc at $r = 400$ arcsec causes some transient disturbances, but these are limited to the outermost disc (this was checked by runs with truncation at $8R_{\rm e} =$ 800 arcsec).

Explicit gravity softening $\epsilon_{\rm grav}$ is used in the calculation of gravitational forces in order to reduce the random force fluctuations caused by the unrealistically small number of particles in simulations, as compared to real galaxies. According to White (1988), this two-body or cell–cell relaxation can manifest as extra heating of the disc and artificial growth or suppression of instabilities. The grid-based calculation of gravitational forces introduces extra softening of the order of $\epsilon_{\rm grid} \simeq 2\pi r/N_\phi$, the effective softening becoming

$$\epsilon \simeq \sqrt{\epsilon_{\rm grav}^2 + \epsilon_{\rm grid}^2}.$$

Softening modifies gravity considerably on scales comparable to ϵ, affecting the local stability properties of the disc. In general, the reactivity of the disc is determined by the fraction of active disc mass to the total mass, the amount of differential rotation and the velocity dispersion of the disc. Values of $Q > 1$ provide local stability against axisymmetric perturbations (Toomre 1964), whereas the disc can still exhibit strong non-axisymmetric responses for Q less than about 2–3 (Julian & Toomre 1966). Gravity softening introduces a stabilizing factor, which to some degree mimics that arising from the finite velocity dispersion. Especially $\epsilon > \epsilon_{\rm cr} = \lambda_{\rm cr}/2\pi{\rm e} \approx 0.0585\lambda_{\rm cr}$, where

$$\lambda_{\rm cr} = 4\pi^2 G\Sigma/\kappa^2 \qquad (2)$$

is the critical wavelength (Toomre 1964), already assures local stability even in the absence of random motions (Miller 1971). Ideally, ϵ should be even smaller than $\epsilon_{\rm cr}$, so that the effective Q has correspondence with the assigned velocity dispersion. Romeo (1994) suggests $\epsilon < e/5\,\epsilon_{\rm cr}$ for the simulation to have realistic stability properties.

The requirement of the suppression of relaxation prevents the use of very small ϵ. Also, improving the grid resolution eventually leads to excess CPU-time consumption. As a compromise we have chosen $\epsilon_{\rm grav} = 2.5$ arcsec as our standard value in connection with $N_\phi = 48$, whereas in the simulations with improved grid resolution, $N_\phi = 108$, we employ $\epsilon_{\rm grav} = 1.25$ arcsec. In what follows these two $N_\phi/\epsilon_{\rm grav}$ combinations are referred as 'coarse resolution' and 'improved resolution'. Fig. 2 plots the relation between $\lambda_{\rm cr}$ and ϵ, indicating that at least between 30–200 arcsec we have $\epsilon < \epsilon_{\rm cr}$ in the runs with improved resolution. However, even these choices of ϵ imply rather large particle numbers. For 2D systems, the theoretical estimate for relaxation time is (White 1988)

$$T_{\rm rel} = \frac{\sigma^3 \epsilon}{5\Sigma G^2 m}, \qquad (3)$$

where m stands for mass of the individual particle and $\sigma = \sqrt{\sigma_{\rm r}\sigma_{\rm t}}$. The relaxation time is thus directly proportional to N and ϵ, and if the rotation curve and Q are fixed, to $M_{\rm d}$. This formula should be a valid approximation also for our 3D system, as the vertical scaleheight is comparable to vertical gravity resolution (White 1988). According to equation (3) (see Fig. 3), at least $N = 4 \times 10^6$ particles would be needed for the relaxation time to exceed the typical length of the simulations (1.5 Gyr) beyond $r = 15$ arcsec. However, previous studies (Thomasson, Donner & Elmegreen 1991) suggest that for the cloud-in-cell force evaluation, which is also used in our code, equation (3) overestimates the relaxation by about a factor of 5. Therefore the use of $N = 4 \times 10^6$ should assure marginal suppression of relaxation beyond about $r =$ 5 arcsec.

To check empirically the possible presence of relaxation, Fig. 3(b) compares the evolution of velocity dispersion in the innermost disc for N in the range of $6 \times 10^4 - 4 \times 10^6$. Clearly, the heating of the disc is very sensitive to N. However, it is evident that this heating is not in accordance with the cell–cell relaxation,

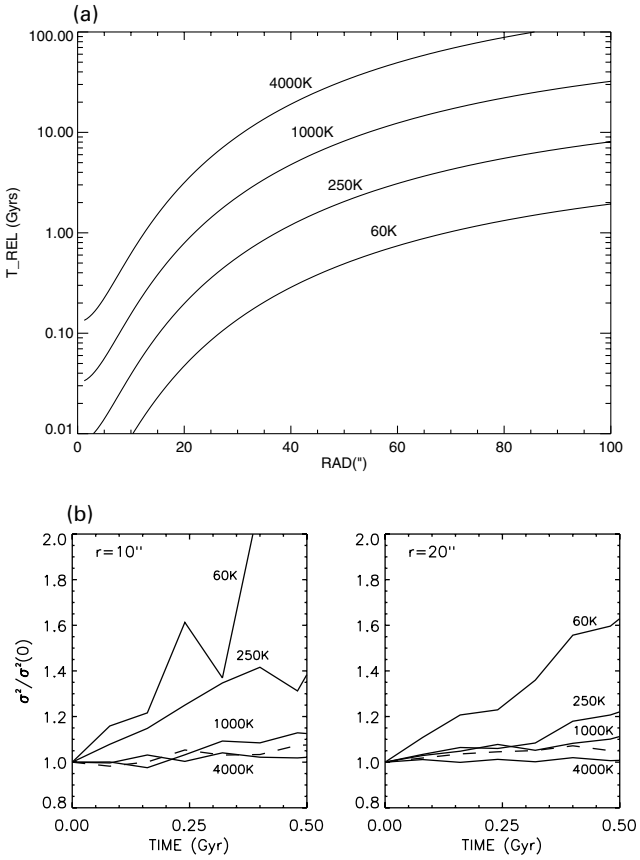

Figure 3. (a) Relaxation time estimates for our simulations, according to the 2D formula of White (1988). Solid lines denote relaxation times $T_{\rm rel}$ for $M_{\rm d} = 0.333$ and $Q = 1.5$, for various particle numbers. Both explicit softening, $\epsilon_{\rm grav} = 1.25$ arcsec, and grid softening with $N_\phi = 108$ are included. For $\epsilon_{\rm grav} = 2.5$ arcsec and $N_\phi = 48$ arcsec, $T_{\rm rel}$ is increased by a factor of about two. For $M_{\rm d} = 0.5$, $T_{\rm rel}$ is also approximately doubled as compared to $M_{\rm d} = 0.333$. (b) Relative increase of radial velocity dispersion in simulations with $M_{\rm d} = 0.333$, during 0.5 Gyr isolated evolution, for $r = 10$ and 20 arcsec. Solid lines are for simulations with coarse resolution, for various values of N, while the dashed line refers to improved resolution, with $N = 4 \times 10^6$.

which would indicate

$$\mathrm{d}\sigma^2/\mathrm{d}t \simeq \sigma^2/T_{\rm rel} \propto 1/N. \quad (4)$$

For example, for $N = 250 \times 10^3$, equation (3) would predict $T_{\rm rel} \approx 0.1$ Gyr for $r = 10$ arcsec, whereas the actual increase in σ^2 corresponds to $T_{\rm rel}$ which is about a factor of 15 longer. Also, the observed relative increase in σ^2 is roughly proportional to $1/\sqrt{N}$, indicating that the heating is mostly the result of amplified N-particle noise, and not of random force fluctuations. The likely cause for the unexpected weakness of the relaxation in the innermost disc is the explicit gravity softening, which apparently suppresses force fluctuations more efficiently than implied by White's formula. In any case, even if the contribution of cell–cell relaxation were totally insignificant, large N of the order of 10^6 helps to keep the heating arising from amplified noise small.

To illustrate the strong effect of softening on the expected stability properties, Fig. 4 plots the maximum growth factors (MGF) for swing amplification for the $M_{\rm d} = 0.333$ disc. Swing amplification is considered a dominant amplification mechanism (Toomre 1981) in galactic discs, describing the process whereby spiral density perturbations grow in amplitude when their pitch

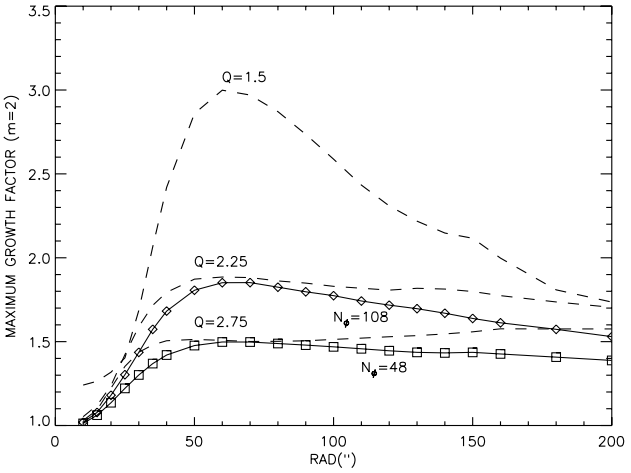

Figure 4. The maximum growth factor (MGF) for $m = 2$ perturbations in the simulation disc with $M_{\rm d} = 0.333$. Dashed lines denote values of MGF as a function of radius for different values of Q, calculated as in Toomre (1981), by taking into account only the stellar velocity dispersion. Solid lines with symbols denote estimates including combined effects of softening + velocity dispersion ($Q = 1.5$), calculated as in Sellwood & Carlberg (1984). Squares and diamonds stand for $N_\phi = 48$, $\epsilon_{\rm grav} = 2.5$ arcsec and $N_\phi = 108$, $\epsilon_{\rm grav} = 1.25$ arcsec, respectively.

angle decreases: maximal amplification is obtained when leading waves are reflected to trailing ones near their corotation. In the calculation of curves of Fig. 4 for our softened disc, we have adopted the same approximation as in Sellwood & Carlberg (1984): the effective gravity reduction factor F in the swing amplification equation (Toomre 1981) is represented by $F = F_{\rm LSK} \times F_{\rm soft}$, where $F_{\rm LSK}(Q,k)$ stands for the Lin–Shu-Kalnajs reduction factor, describing the influence of non-zero velocity dispersion, and $F_{\rm soft} = \exp(-\epsilon k)$ is the reduction factor arising from softened gravity, with k denoting the radial wavenumber of the shearing perturbation. According to Fig. 4, the MGF of $m = 2$ perturbations reaches a maximum of about 1.8 at $r \approx 60$ arcsec, decreasing slowly for the outer disc. For comparison, the maximum MGF in the presence of velocity dispersion alone ($Q = 1.5$) would be about 3, indicating the expected strong stabilizing effect of softening. For the coarser grid, the maximum of MGF is reduced to about 1.5. To obtain MGFs similar to those in the case of softened gravity, Q should be increased to about 2.25. For $M_{\rm d} = 0.5$ the maximum of MGF is about 3.2 for the softened case: in this case the softening in combination with $Q = 1.5$ corresponds roughly to an effective $Q_{\rm eff} \approx 2$. Thus, providing that the effects of softening really mimic the increased disc temperature, the stability properties of our softened discs should approximate stellar discs with $Q_{\rm eff} \approx 2.0$–2.25.

In the next section we study the evolution of the system with the help of a Fourier transform of the disc surface density in polar coordinates (r,θ) (see, e.g., Masset & Tagger 1997). We calculate for our exponentially spaced radial bins, centred at distance r_j, the coefficients

$$W_{\rm c}^{\rm m}(r,t) = \frac{1}{n_j}\sum_i \cos(m\theta_i), \quad (5)$$

$$W_{\rm s}^{\rm m}(r,t) = \frac{1}{n_j}\sum_i \sin(m\theta_i), \quad (6)$$

where the summation is over the n_j particles with radial coordinates at the bin corresponding to r_j. This is done separately

for $m = 1$–8. The amplitude spectra are obtained from the Fourier transform of $W_c^m + iW_s^m$ with respect to time, yielding relative perturbed density as a function of frequency ω and radius. In our plots we use the pattern speed, $\Omega_p = \omega/m$. We also display plots of the normalized Fourier amplitude, $A_m(r,t) = 2\sqrt{(W_c^m)^2 + (W_s^m)^2}$, as well as the cosine transform, $W_c^m(r,t)$, to characterize the radial propagation of perturbation densities. In addition, logarithmic spiral decompositions were examined, with amplitudes calculated from

$$A(m,p,t) = \frac{1}{n}\sum_{i=1}^{n} \exp[i(m\theta_i + p\log r_i)]. \quad (7)$$

The inclination angle of the spiral component with respect to radial direction is $\tan^{-1}(p/m)$, positive (negative) values of p corresponding to trailing (leading) waves. Since the spiral structures seen in simulations exhibit very different characteristics at the inner and outer parts of the disc, we calculated these coefficients separately for $r < 50$ arcsec and $r > 50$ arcsec; n denotes the number of particles in the region in question.

3 ISOLATED VERSUS PERTURBED EVOLUTION

3.1 Isolated evolution

In the absence of external perturbation our standard simulation disc is stable against the formation of strong large-scale structures (Fig. 5). Weak multiarm spirals form in the outer parts, with larger multiplicity for $M_d = 0.333$ as compared to $M_d = 0.5$. This behaviour is in accordance with theoretical expectations: swing amplification maximum growth factors in the outer discs are strongest for $m = 4$–5 and for $m = 3$–4, if $M_d = 0.333$ and 0.5, respectively. In both cases $m = 2$ spirals prevail in the inner parts: for $M_d = 0.5$ these spirals are stronger and more open, and tend to have an oval central component. Formally, MGFs for higher values of m exceed those for $m = 2$ also in the interior, but waves with higher values of m always possess ILRs and thus cannot easily reach the central regions.

The simulations in Fig. 5 were performed with $N_\phi = 108$ grid resolution and $\epsilon_{grav} = 1.25$ arcsec. In simulations with coarser resolution ($N_\phi = 48, \epsilon = 2.5$ arcsec) the overall evolution was rather similar, except that the inner structures were somewhat weaker and the multiplicity of the outer spirals was slightly less. Both effects are in accordance with the expected change in the strength of the swing amplification. We also estimated the swing amplification efficiency directly from simulations. The ratio between the total amplitudes on trailing and leading sides was about 1.4 and 1.25, for the simulations with improved and coarser resolutions, respectively. This was measured for $r < 50$ arcsec during the first 0.5-Gyr period, when the disc had not yet developed any strong structures. This difference between the trailing/leading bias in runs with different resolution is in rough accordance with the MGFs estimated in the previous section.

The evolution of the disc is studied in more detail in Fig. 6, displaying the amplitude spectra of $m = 2$ surface density perturbations for $M_d = 0.333$ and 0.5. For both disc masses, the evolution of the outer disc is characterized by numerous distinct waves with different pattern speeds. If spectra from shorter time intervals are examined, slightly different frequencies are dominant, indicating that no actual long-lived modes are set up. There are also no signs of any coupling between the frequencies of waves. Waves possessing low pattern speed are confined between their ILR and OLR, as expected. Their maximum amplitudes seem to be concentrated near ILR, suggesting radial propagation of wave packets. Also, strong waves are seen at higher pattern speeds, lacking ILR. It is just these waves which are easily visible in the direct density plots of the inner disc.

The radial propagation of amplitudes associated with individual wave packets is discerned in Fig. 7(a) displaying the time evolution of the normalized $m = 2$ amplitudes at various distances for the $M_d = 0.333$ run. A logarithmic radial scale is used, to emphasize the innermost regions. Both outward and inward drifting amplitude peaks are seen, the latter dominating in the inner disc. Inspection of the $m = 2$ phase information shows that these features correspond to individual travelling wave packets. Most of the waves originate from $r = 50$–150 arcsec, where the

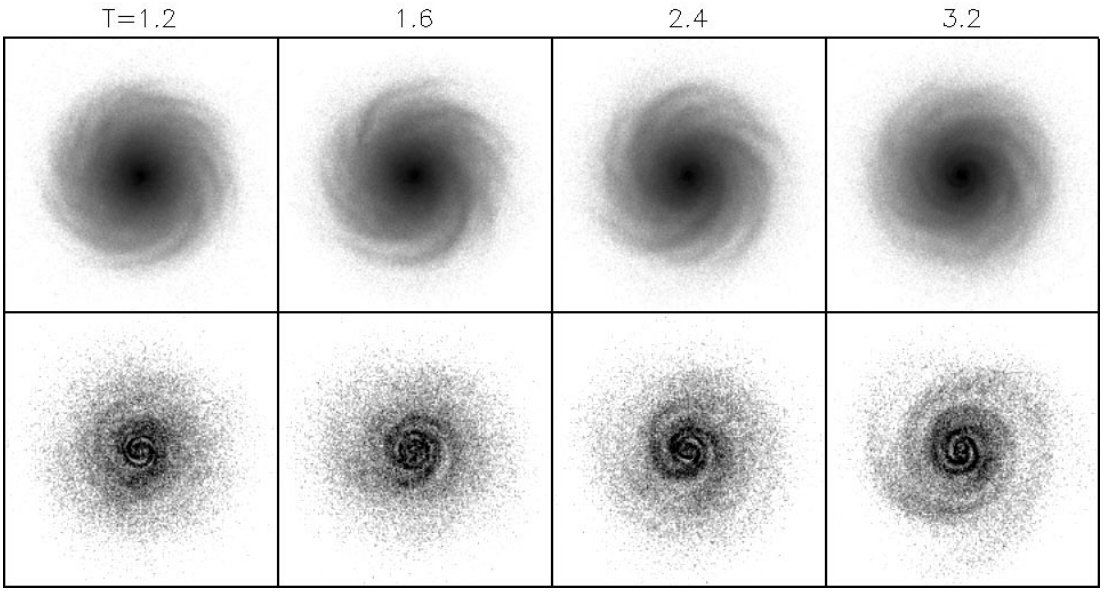

Figure 5. Evolution of the simulation disc during an isolated evolution of 3.2 Gyr with $M_d = 0.333$. The size of the upper frames is 1200×1200 arcsec, while the lower frames show the inner 200×200 arcsec region. $N = 4 \times 10^6$ particles are simulated with the improved resolution.

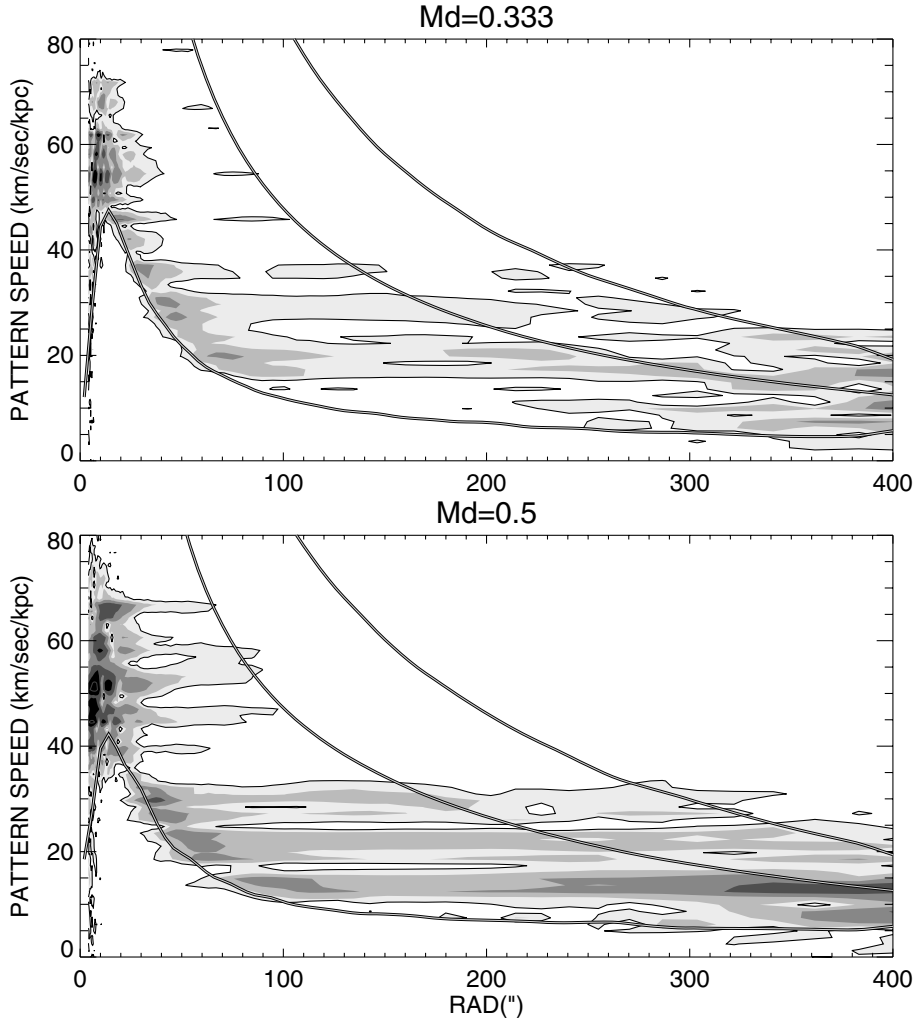

Figure 6. Amplitude spectrum for the $m = 2$ Fourier component of the disc surface density in the isolated runs calculated from the time interval 0.8–3.2 Gyr. The solid lines (from left to right) denote the $\Omega - \kappa/2$, Ω, and $\Omega + \kappa/2$ curves: these have been constructed from the radial forces at $T = 2$ Gyr. For an $m = 2$ wave with a constant pattern speed, intersection with these curves corresponds to the inner Lindblad resonance, the corotation resonance, and the outer Lindblad resonance, respectively. The resolution of the pattern speed is about $1.2\,\mathrm{km\,s^{-1}\,kpc^{-1}}$. Contour levels correspond to $A_{\min} \times 2^{\mathrm{i}}$, with $A_{\min} = 0.005$ and $i = 0$–5. The $m = 2$ amplitude is normalized to $m = 0$ component.

swing amplification MGFs are largest. A remarkable feature of the waves seen in the inner disc is their persistence and saturation at rather high amplitudes. For example, the recurrent amplitude maxima seen in the inner disc have amplitudes reaching about 0.1 and 0.2 at $r \approx 15$ arcsec, for $M_{\mathrm{d}} = 0.333$ and 0.5, respectively. Also the higher-m components in the outer disc retain their amplitudes of the order of 0.1–0.2 at $r \sim 400$ arcsec. There are no signs of the decay of spiral amplitudes during the studied 3.2-Gyr time-span, even if this corresponds to several hundreds of dynamical times for the innermost disc (see Fig. 7b). This kind of behaviour is seldom seen in *N*-body simulations, where spiral structures usually dissolve via the heating of the disc, unless some cooling mechanism, as in Sellwood & Carlberg (1984), is applied. Nevertheless, in the current large-*N* simulations, the increase in Q is only about 25 per cent even for $r = 15$ arcsec during 3.2 Gyr, and there is no apparent change in the disc stability properties.

The slopes of the inward and outward drifting amplitude maxima seen in Fig. 7(a) are compatible with the characteristic group velocity, $v_{\mathrm{char}} = \kappa/k_{\mathrm{cr}}$, which equals about 7.5 kpc/100 Myr, or about 160 arcsec/100 Myr for $r = 80$ arcsec, where v_{char} has its maximal value in our models. To be more quantitative, Fig. 8 follows in detail the radial evolution of one individual wave packet, in the run with $M_{\mathrm{d}} = 0.5$. As in Fig. 7(a), the shading indicates the strength of the normalized $m = 2$ amplitude, $A_2(r,t)$. Also shown, with overplotted contours, is the $m = 2$ cosine transform, $W_{\mathrm{c}}^{(2)}(r,t)$. The maximum contour values correspond to a spiral density crest sweeping through a fixed direction in the disc. The slope of the contours gives an indication of the pitch angle of the wave: a trailing (leading) wave corresponds to forward (backward) leaning slopes, while vertical alignment corresponds to a bar/oval. An individual packet is discerned as a series of coherently propagating fronts, and the time-distance between the crests measures the pattern speed of the packet, $\Omega_{\mathrm{p}} = (2\pi)/m\Delta T$, where ΔT is the time difference between two successive maxima. The packet shown in the figure does not quite evolve as a Lin–Shu wave, as its pattern speed gradually increases from about 15 to $30\,\mathrm{km\,s^{-1}\,kpc^{-1}}$ during its inward propagation between $r = 300$ and $r = 50$ arcsec. However, inside 50 arcsec the pattern speed remains practically constant. Nevertheless, the radial propagation is quite well approximated by the group velocity $v_{\mathrm{g}} = \partial[\omega - m\Omega(r)]/\partial k$ calculated from the

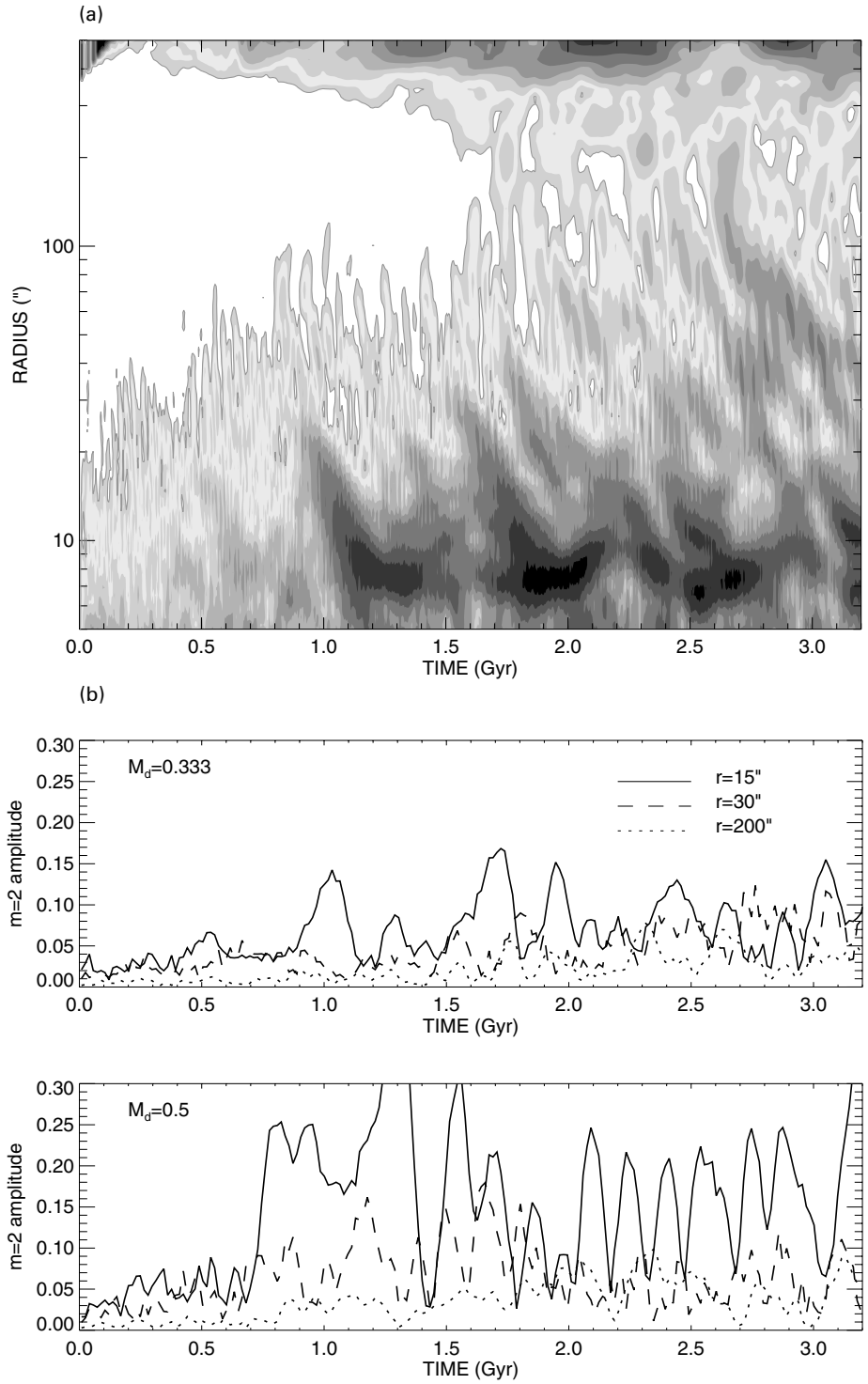

Figure 7. (a) Evolution of the normalized $m = 2$ Fourier amplitude, $A_2(r, t)$, as a function of time and distance in the isolated run with $M_{\rm d} = 0.333$. Smallest and largest contour levels are 0.02 and 0.2, respectively. (b) Fourier amplitude A_2 at three selected distances (15, 30 and 200 arcsec), for $M_{\rm d} = 0.333$ and 0.5.

short-wave branch of the Lin–Shu dispersion relation (Binney & Tremaine 1987).

Fig. 9. provides views of the evolution of wave packets near the centre, plotting the $m = 2$ cosine transform of density as a function of time and radius for the innermost 50 arcsec (upper frames). The cases $M_{\rm d} = 0.333$ and 0.5 are both shown. In the lower frames, the morphology of the inner disc is shown on selected instants of time. It is clearly seen how some individual packets reach the centre and then reflect back as a leading packet with the same pattern speed, giving rise to an interference between the ingoing and outgoing waves. The occasional leading morphology of the innermost arms is visible also in the direct density plots, being especially pronounced in the case of the more massive disc.

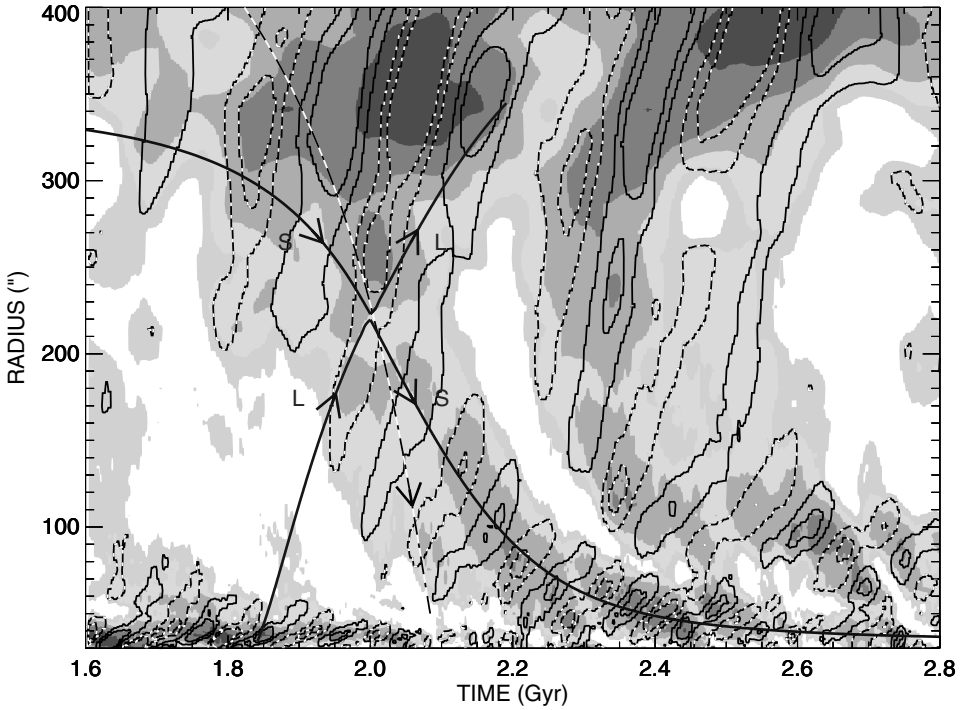

Figure 8. Example of the radial propagation of a single wave packet, for an isolated run with $M_d = 0.5$. The normalized $m = 2$ Fourier amplitude is represented by shades of grey, while the contours correspond to the $m = 2$ cosine transform, $W_c^{(2)}(r, t)$, indicating the times and locations when a tidal crest (solid contours) passes a given fixed direction in the disc. Overplotted curves display the expected radial propagation of a wave packet, calculated from the group velocity according to Lin–Shu dispersion relation, for $\Omega_p = 20\,\mathrm{km\,s^{-1}\,kpc^{-1}}$ and $Q = 1$. Symbols S and L stand for short and long branch of the dispersion relation, respectively, while the arrows indicate the expected direction of the propagation for trailing perturbations. For this Ω_p, the ILR, CR and OLR distances are at $r \approx 40$, 220 and 350 arcsec, respectively. Dash-dotted line denotes the inward propagation according to v_{char}.

Above we saw that the individual packets seen in simulations do not have fixed pattern speeds. Also, the shapes of the spirals deviate from those derived from the Lin–Shu dispersion relation. Rather, their shape seems to be related to the critical wavenumber at each distance, so that $m\partial\phi_0/\partial r \approx k_{cr}$, where ϕ_0 stands for the phase of the maximum density at distance r. This relation implies that the radial distance between the successive spiral arms adjusts close to λ_{cr}. This result was first found by Donner & Thomasson (1994) in simulations with globally unstable disc models (a similar tendency was also remarked by Sellwood & Lin 1989). In their case this dependency was found to be approximately valid for a large-scale $m = 2$ mode (extending about 4 radians in azimuth), before the spirals eventually disappeared as a result of the heating of the disc. Fig. 10 gives a similar example from the current simulations, corresponding to the strong packet visible in Fig. 9(a) just before its reflection from the centre. Since the wave packet retains a practically constant pattern speed during the propagation near the centre ($r < 30$ arcsec), its shape can be effectively determined by superposing snapshots of the $m = 2$ density component from several time-steps, in a coordinate system rotating with the pattern speed of the wave. Besides showing the critical spiral, Fig. 10 also displays the shape calculated from the short-wave branch of the linear Lin–Shu dispersion relation. This shape has $k > k_{cr}$, giving a much too tightly wound pattern. Thus, present simulations confirm that the above purely empirical formula $k \approx k_{cr}$ can describe the shape of a spiral feature suprisingly accurately over a relative distance range of even about 10, when the phase of the spiral varies by almost 10 radians. Note, however, that the shape presented in Fig. 10 is a superimposed image of the wave over its inward propagation: in any single instant of time the wave packet is more limited in its radial extent.

Inspection of the $m = 2$ logarithmic spiral decompositions for the above simulations indicate that coherent signals with smaller pitch angles (corresponding to $k > k_{cr}$) are also present, indicating that travelling disturbances do not necessarily always follow the above critical shape. Nevertheless, in all cases where individual spirals appear strong enough so that their shape can be determined, the above k_{cr} dependence seems to be valid.

The above analysis demonstrates that our initial disc model, although globally stable against large-scale instabilities, has fairly reactive inner portions exhibiting recurrent $m = 2$ wave packets. These maintain their strength during the simulation, most likely because as a result of the large N, the increase in the velocity dispersion of the disc is quite slow. The radial propagation speeds of the packets can be approximated with those calculated for Lin–Shu waves, although the packets seem to be unable to maintain fixed pattern speed during their evolution. Also, the shapes of at least the strongest spirals deviate significantly from the shape derived from the linear Lin–Shu dispersion relation, even in the region where the pattern speeds are fairly constant. Reflection of individual packets from the centre were also seen. Because of the relative weakness of swing amplification, the leading waves have amplitudes comparable to the trailing packets, so that they are visible also in direct density plots. No permanent modes are established, however. We will next study the response of the simulation disc to external perturbation.

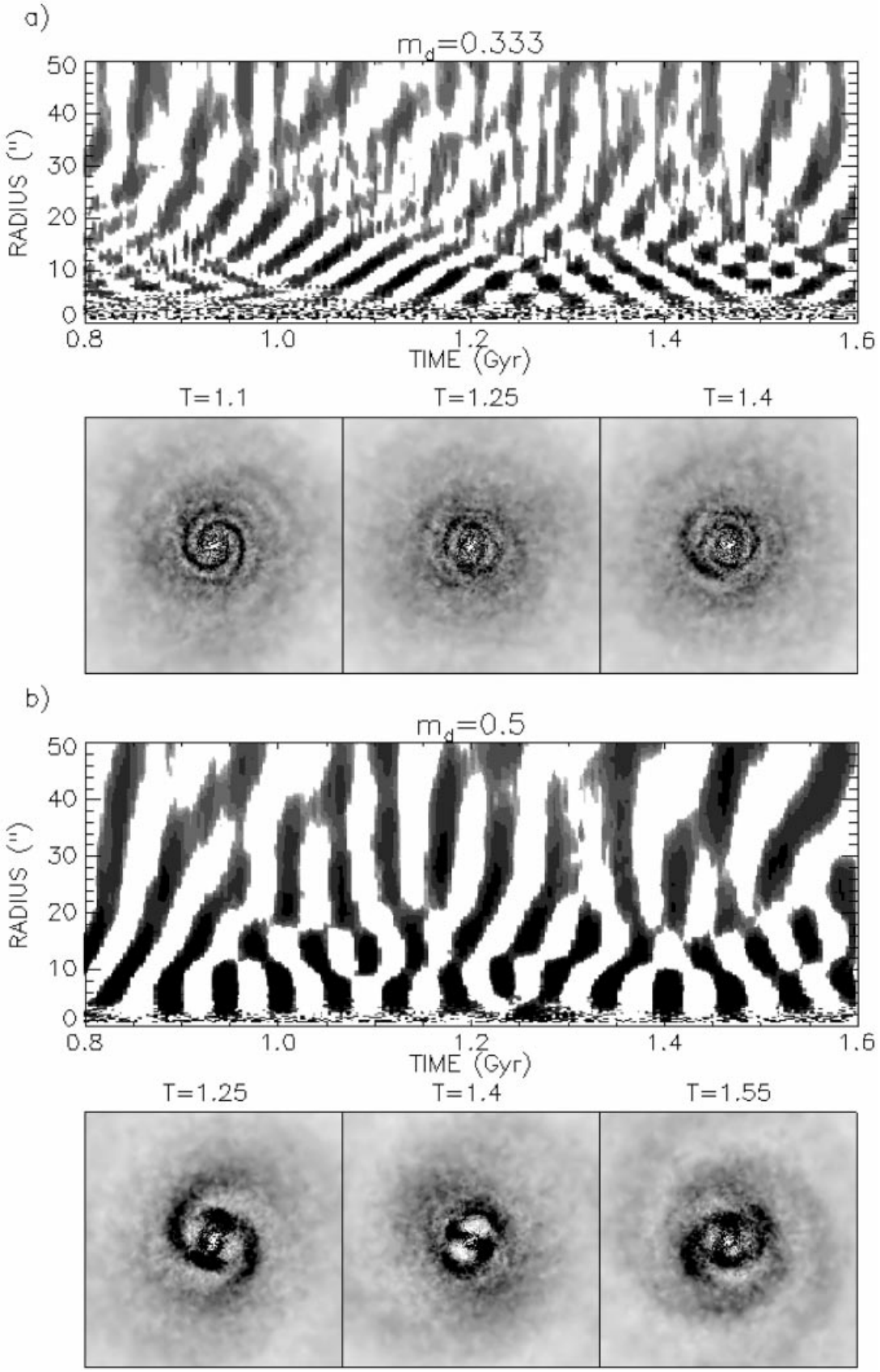

Figure 9. Reflection of wave packets from the centre. The upper frames display the $m = 2$ cosine transform, $W_c^{(2)}(r, t)$, while the lower frames display the morphology of the innermost 100×100 arcsec region at selected instants of time. In (a) $M_d = 0.333$ and in (b) $M_d = 0.5$.

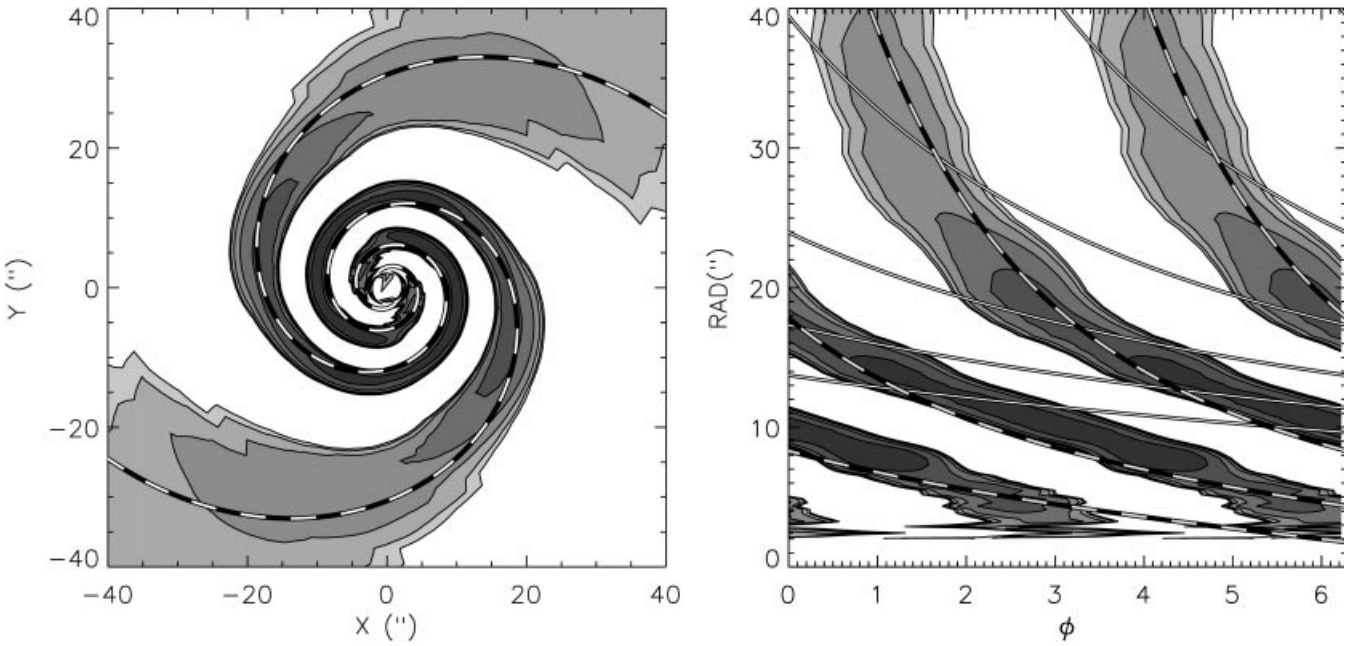

Figure 10. Example of the shape of an $m = 2$ wave packet, seen in the isolated run of Fig. 9a at $T \approx 1$ Gyr. The plot has been obtained by superposing the $m = 2$ density components from approximately 50 different time-steps between $T = 0.9$ and $T = 1.1$, in a coordinate system rotating with the pattern speed of the packet, $\Omega_p = 57\,\mathrm{km\,s^{-1}\,kpc^{-1}}$. In the right-hand panel, the same packet is displayed in polar coordinates. The black-white dashed lines indicate the shape of the critical spiral, having at each distance the radial wavenumber $k = k_{cr}$, while the solid line in the polar plot represents the shape of the short-branch wave calculated from the linear Lin–Shu dispersion relation.

3.2 Perturbed evolution

In our tidal models for M51 (Paper I) the principal perturbation, capable of accounting for the observed spiral structure, at least beyond about 50 arcsec, takes place when the companion crosses the disc plane of the primary galaxy about 400–500 Myr before the present time, at a distance of about 600 arcsec. This crossing, as viewed in the sky plane, is assumed to occur near south, at PA $\approx 155°$. In Paper I two different types of encounter histories, differing in the crossing direction, were compared. In a single-passage model with a nearly parabolic relative orbit, the southern crossing occurs away from the observer, and at the current time the companion is far behind the primary galaxy. However, in Paper I an alternative possibility was favoured, with the southern crossing toward the observer, indicating lower current eccentricity and another more recent disc-plane crossing, about 50–100 Myr before the present time, so that the companion can attain its current velocity away from the observer. This later crossing occurs at a distance of about 400–500 arcsec. This orbit was suggested to represent the final portion of the orbit which has significantly shrunk and circularized during the long-term encounter history of the pair.

Fig. 11 displays both the multiple and single-encounter models at the present time, whereas the time evolution of the former is shown in Fig. 12. Compared to the models with similar geometries presented in Paper I, the particle number has been increased and the grid resolution is improved. Before perturturbation the disc was evolved in isolation for about 1 Gyr, during which time it developed weak multi-armed structures as shown in the previous subsection. Following the companion crossing of the primary disc plane, strong $m = 2$ tidal arms overwhelm all pre-existing outer structures. As time passes, the arms become increasingly wrapped. At $T \approx 400$–500 Myr after the southern disc-plane crossing they extend continuously to about 10 arcsec, completing about the same number of revolutions as the spirals in observations. Also, a small oval is seen in the centre, on the rising part of the rotation curve. The evolution of the single passage model is nearly identical until $T \approx 400$ Myr, when the second crossing occurs in the bound model, accounting for most of the difference in the present outer morphology. On the other hand, the inner portions of the disc are practically identical in both models. In Paper I the corresponding models remained practically featureless inside 50 arcsec. When the perturbation is followed past the nominal observing time, the primary galaxy becomes increasingly disturbed.

Because of the large inclination of the companion orbit, the external forcing is fairly slow. Nevertheless, its Fourier spectrum consists of a broad range of different forcing frequencies. Because of the relatively short time-span of the perturbation, it is not easy to analyse the frequencies of the waves excited in the disc. Low-resolution amplitude spectra for successive 150 Myr time-intervals indicate that the strongest initial response takes place at low pattern speeds, being comparable to the angular speed in the outer disc, $\sim 10\,\mathrm{km\,s^{-1}\,kpc^{-1}}$. After that the perturbation gradually extends inward and signals at higher frequencies are seen. The $m = 2$ amplitude spectrum for the whole perturbed evolution (600 Myr, Fig. 13) supports the impression that progressively higher pattern speeds are excited in the interior, with maximum amplitudes at each frequency being attained near the $\Omega - \kappa/2$ curve. Also shown in Fig. 13 is the amplitude spectra of isolated evolution, calculated for a corresponding 600 Myr time-span, in order to have the same resolution and noise level. Except for $r < 15$ arcsec, the perturbed case shows much-increased amplitudes. Also, the amplitudes inside 15 arcsec join continuously to the outer large amplitude levels. For the single-encounter model of Fig. 11, the $m = 2$ amplitude spectrum is practically identical to

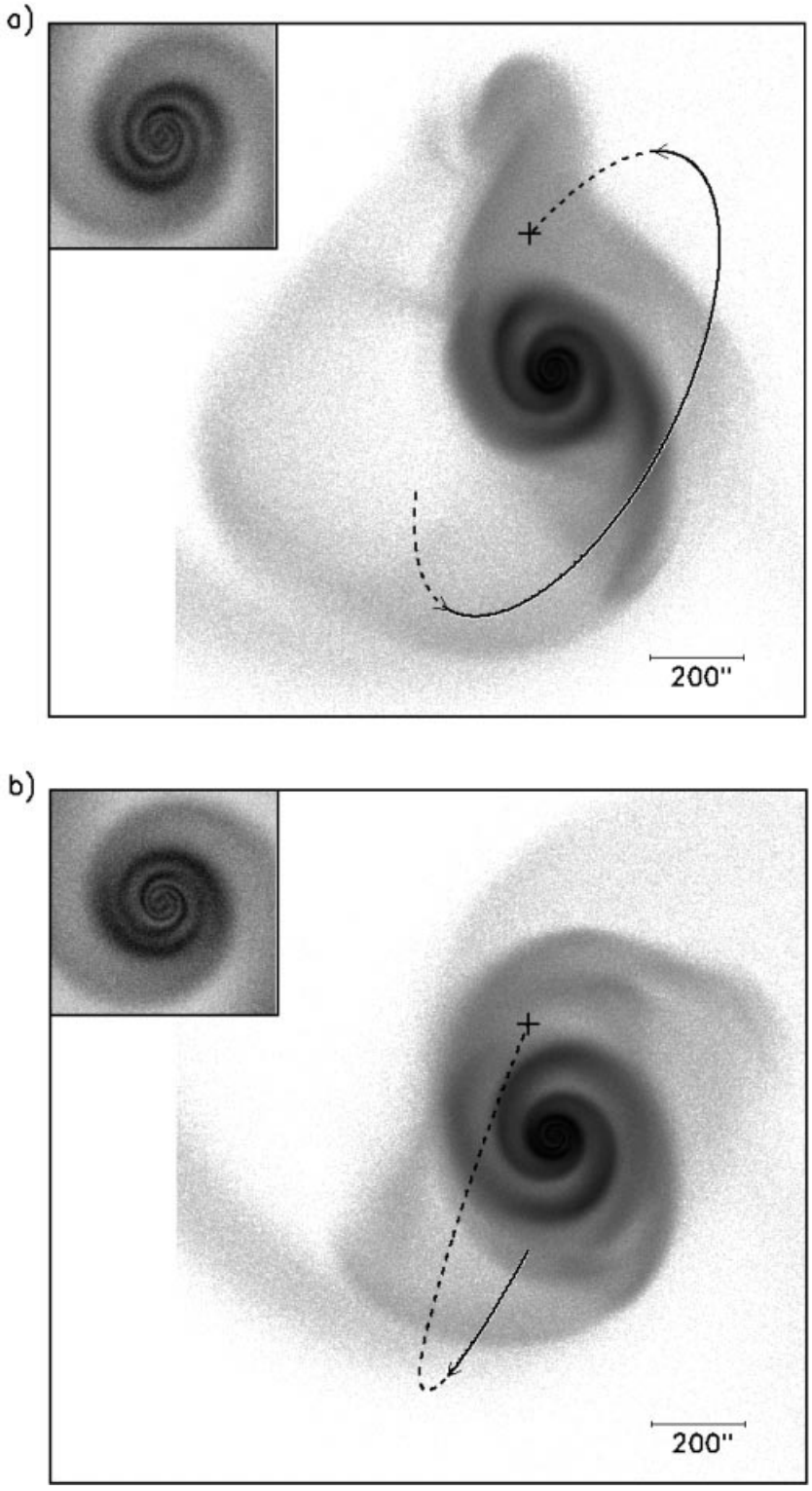

Figure 11. Two types of models for the interaction between M51 and its companion NGC 5195. Projection to the sky-plane is shown with 20° inclination and 170° major axis position angle. The small inserts display the inner 200×200 arcsec region. In (a) a bound model is shown, with a solid line indicating the portion of the companion orbit on the side nearer to the observer with respect to the disc of M51. In (b) a nearly parabolic single passage is displayed. In both cases the separation and the projected velocity correspond to observations at $T = 450$ Myr. Simulations employed 4×10^6 particles and the coarser grid resolution.

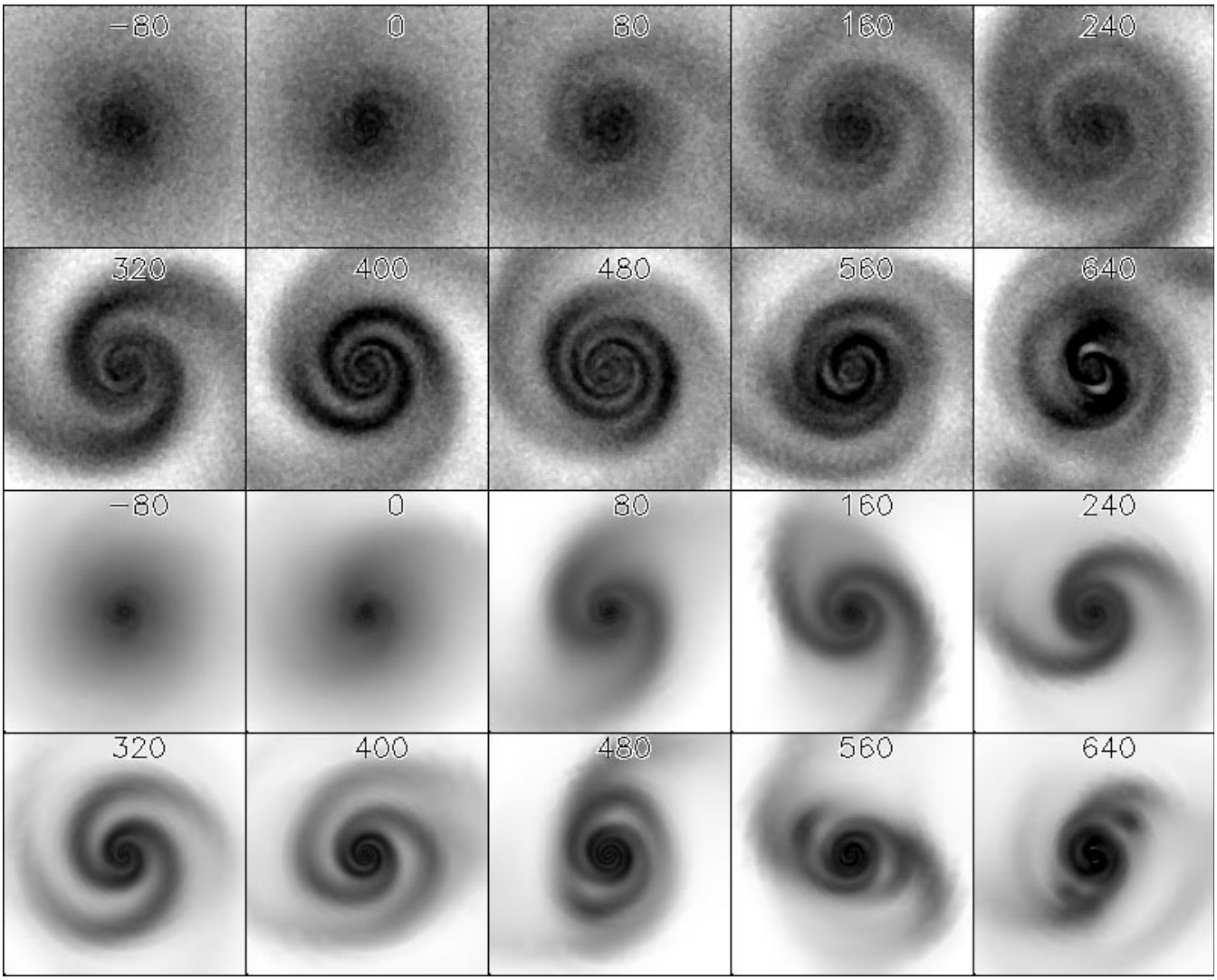

Figure 12. Time evolution of the bound model of Fig. 11(a). In the upper frames the inner 200 × 200 arcsec region is followed, while the lower frames cover 600 × 600 arcsec. Times are in Myr, calculated from the southern disc-plane crossing.

that of $M_{\rm d} = 0.333$ shown in the plot, in spite of the approximately 30 per cent faster passage of the companion.

The time-evolution of $m = 2$ amplitudes at various distances is studied in Fig. 14. In addition to $M_{\rm d} = 0.333$ and 0.5, the case with $M_{\rm d} = 0.2$ is also shown, to highlight the dependency of the propagation of the tidal wave on the disc mass. In all cases there is a strong increase in amplitude within 100 Myr of the southern disc-plane crossing. This increase takes place almost simultaneously for all $r > 100$–200 arcsec. These increased amplitudes are related to the formation of the bridge and tail and the outer spiral structure, and correspond to the low pattern speeds in the amplitude spectra. After $T = 100$–200 Myr, the maximum amplitudes are seen to propagate gradually inward, with speed comparable to the characteristic group velocity. The same evolution is seen both for $M_{\rm d} = 0.333$ and 0.5, and as suggested by the larger $v_{\rm char}$, the propagation is faster in the latter case. On the other hand, for $M_{\rm d} = 0.2$ the inward propagation is very weak. In the innermost regions ($r < 80$ arcsec) the propagation speeds are slower, being comparable to those of the packets in the isolated runs near the centre. Also, in this region several separate packets are visible, especially for $M_{\rm d} = 0.5$, and for the somewhat later times in the $M_{\rm d} = 0.333$ simulation. The renewed amplitude peak in the outer disc at $T \approx 500$ Myr is related to the second crossing of the companion: connected to this, a new front of inward propagating amplitudes is seen.

A more detailed view of the radial evolution of the tidal wave is presented in Fig. 15, displaying the combined $A_{\rm m}(r, t)$ (gray-scale shades) and $W_{\rm c}^{\rm m}(r, t)$ (contours) plots for $m = 2$. The single-passage model of Fig. 11(b) is studied, in order to omit the effects of the second crossing. It is clearly seen how the first amplitude peak at $T = 100$–200 Myr is connected to a low-frequency wave, with $\Omega_{\rm p} \approx 15\,{\rm km\,s^{-1}\,kpc^{-1}}$. When this wave approaches its ILR at $r \approx 100$ arcsec, an interesting phenomenon occurs: several new wave packets are initiated, all having about twice as high a pattern speed as the initial one. Even these new wave packets would have an ILR, but since their azimuthal frequency increases during the inward propagation, they are able to slide over the ILR barrier (this sliding corresponds to the increased amplitude levels near the $\Omega - \kappa/2$ curve in Fig. 13). Thus it seems that in this transient process there is no typical mode coupling in the sense that the corotation of the inner wave would correspond exactly to the ILR of the outer wave (Tagger et al. 1987; Masset & Tagger 1997).

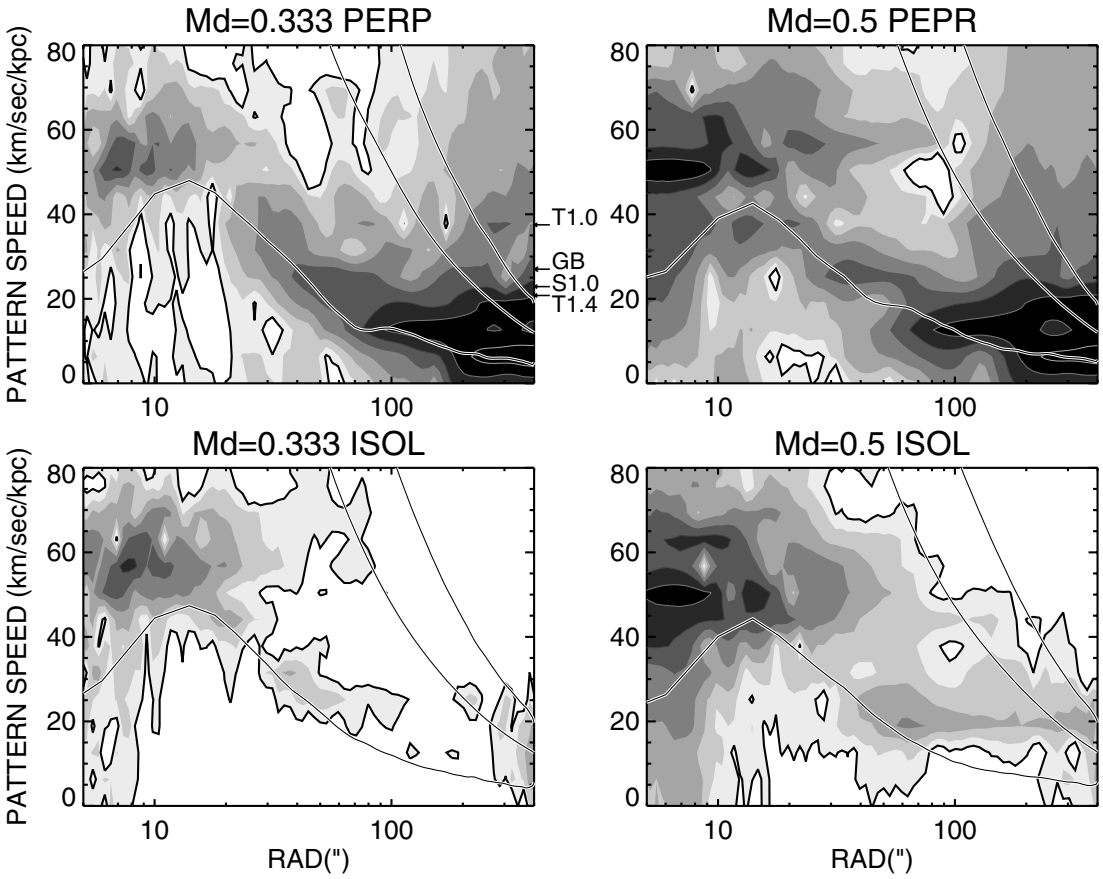

Figure 13. Upper frames display the amplitude spectrum of the perturbed evolution, for 600-Myr interval after the southern disc-plane crossing. Contour levels correspond to $A_{\rm min} \times 2^{\rm i}$, with $A_{\rm min} = 0.005$ and $i = 0$–7. The arrows on the right-hand axis of the $M_{\rm d} = 0.333$ case mark the pattern speeds assumed in density wave fits of Tully (1974b) (T1.0 and T1.4 refer to $Q = 1.0$ and 1.4, respectively) and Shu et al. (1971) (S1.0; $Q = 1$). Also shown is the pattern speed yielding the best morphology in the simulations with colliding test particles by Garcia-Burillo et al. (1993). For comparison, the lower frames show the amplitude spectrum from an isolated run, for the same period of time.

Also seen in Fig. 15 is the interplay between the intrinsic and tidal waves at the region around $r = 10$ arcsec : at most instants of time the intrinsic and external patterns join smoothly together, giving an impression of a continuity of the spiral arms. This is possible, as the azimuthal propagation speeds of the tidal waves are very similar to those of the intrinsic ones in the same region.

The initial shape of the spiral arms forming during the perturbation is also well described by the $k_{\rm cr}$ dependency, as is the case for the isolated spirals. However, as the azimuthal propagation speed increases during the inward progression of the wave, the arms develop smaller pitch angles. Typically, when $k \approx 2k_{\rm cr}$, the adjacent arms may merge together, restoring the $k_{\rm cr}$ dependency at least temporarily. Similar phase shifts of 180° were reported in the simulations of Donner & Thomasson (1994). However, during the later phases the inner spiral segments, moving with higher pattern speeds, separate completely, and the spiral arm is divided into segments each obeying the $k_{\rm cr}$ dependency over smaller radial extents. Evidently, this is connected to the separate packets seen in Fig. 15.

In conclusion its seems that with the assumptions made about the rotation curve, relative disc fraction and the perturbation strength, the inward propagating tidal wave is indeed capable of penetrating to the central regions inside 30 arcsec and of exciting central spirals. However, similar spirals may also be expected during the isolated evolution, provided that the stability properties and rotation curve resemble the above model. Nevertheless, the perturbation seems to be essential to account for the continuity of the structures observed for M51.

3.3 Influence of the rotation curve

All the previous experiments have been performed with a rotation curve which has a very short inner rising part (about 15 arcsec). Our simulations have indicated that, in this portion, the wave packet often has an oval appearance, especially in the case of the more massive disc. To check the effect of the rotation curve on the formation of the oval, a series of experiments was performed by varying the halo core radius $R_{\rm c}$ (the scale of the rising portion is $\sim 2R_{\rm c}$), while the disc density distribution was kept the same as before. Fig. 16 compares the inner morphology of perturbed runs with $R_{\rm c} = 8$, 16 and 32 arcsec. Note that the latter two values yield inner slopes which are not consistent with the rotation curve of M51 but are perhaps even more typical of galaxies in general.

The change of the inner rotation curve modifies the dynamical properties of the inner disc in several ways. First, the critical wavelength increases, as the halo contribution and thus κ decreases. Secondly, in spite of the increased disc contribution, the swing amplification becomes weaker as a result of reduced amounts of differential rotation. Because of this, the strength of inner structures forming in isolated runs is weaker for larger $R_{\rm c}$.

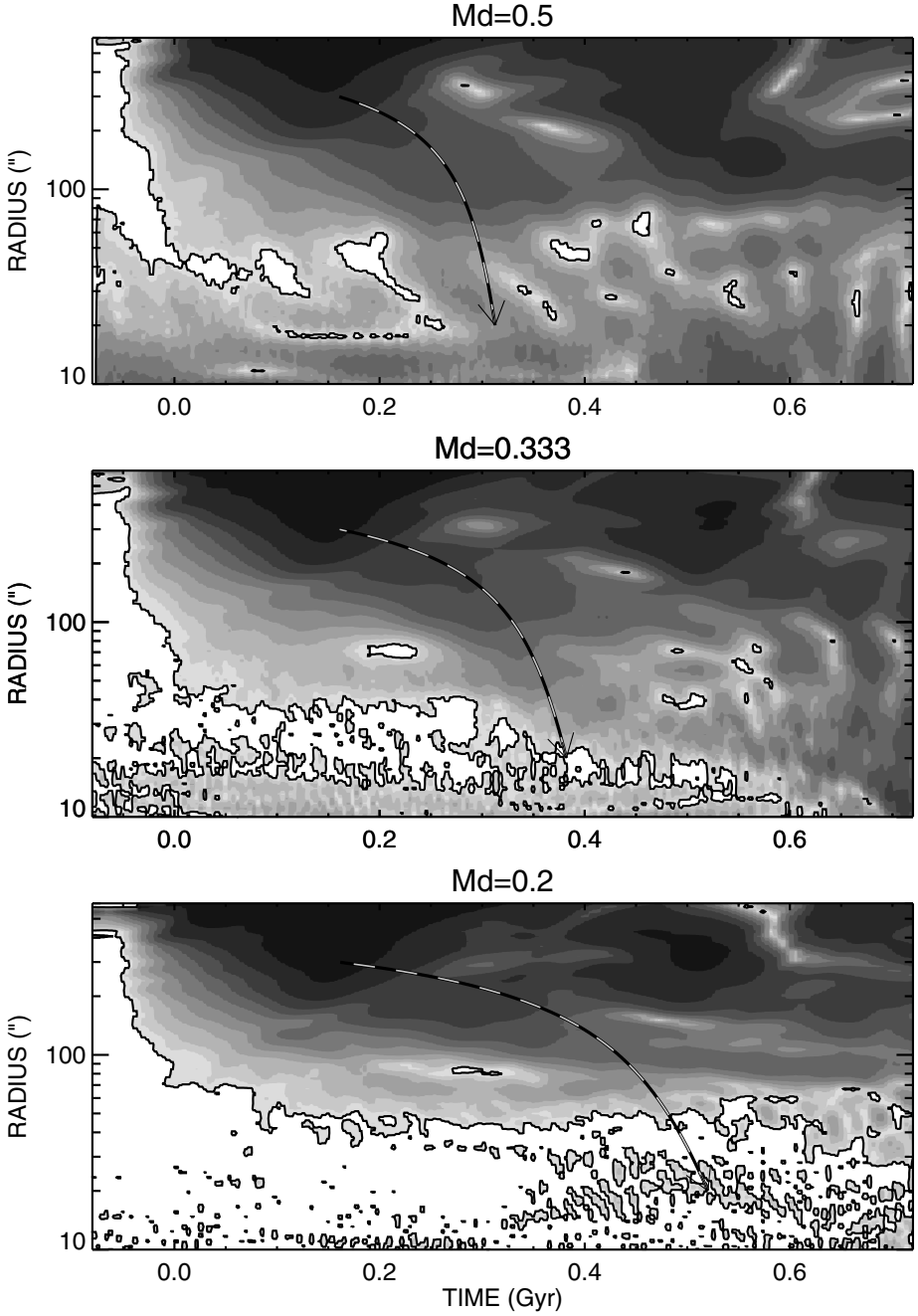

Figure 14. Evolution of the $m = 2$ Fourier amplitude, $A_2(r, t)$, as a function of time and distance in the perturbed runs with $M_d = 0.5$, 0.333 and 0.2. Dashed lines indicate the radial propagation corresponding to v_{char}.

Thirdly, the maximum value of $\Omega - \kappa/2$ is lowered for larger R_c, which in the perturbed case makes it easier for the low frequency $m = 2$ waves to reach the innermost region. This accounts for the stronger response in the case of external perturbation: for example, in the case $R_c = 32$ arcsec, all $m = 2$ waves with $\Omega_p > 13\,\mathrm{km\,s^{-1}\,kpc^{-1}}$ lack an ILR, so that the distortions of the outer disc can propagate directly to the central regions. This manifests as a formation of a central bar, very much like the interaction-induced formation of large-scale bars (Noguchi 1987, 1996; Salo 1991). Nevertheless, the excited waves in the interior are again similar to those which are present, albeit much weaker, also in the isolated case. The central oval is likely to be related to large λ_{cr}, as was also the case with larger M_d. Note that, in these runs with larger R_c, any artificial effects arising from the use of softened gravity and grid are reduced as compared to the standard value $R_c = 8$ arcsec: this is partly because larger structures form, but also partly because the effects of softening depend on ϵ/λ_{cr}.

3.4 Influence of particle number

Fig. 16 also compares perturbed experiments with different total N. Just the innermost 200 by 200 arcsec are displayed, the outer spiral arms being very similar in each case. With increased N,

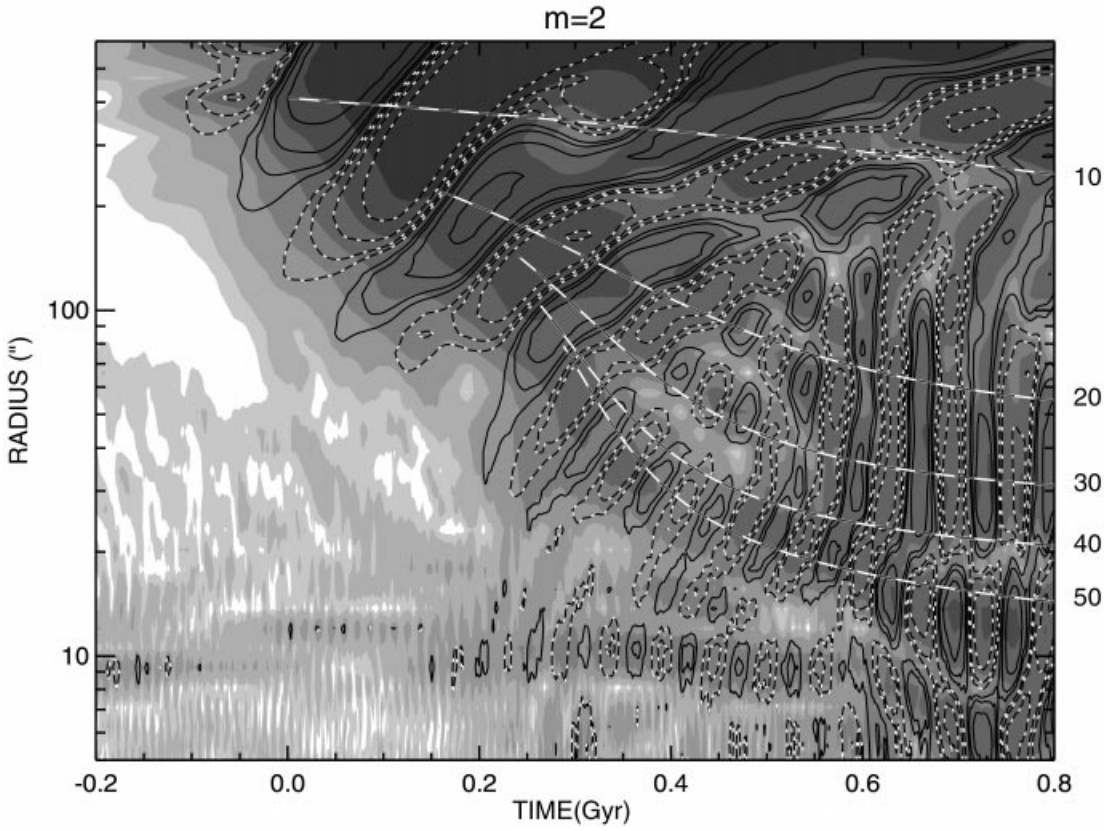

Figure 15. Propagation of tidal packets in the parabolic model of Fig. 11(b). Shades of grey correspond to A_2, and contours to $W_c^{(2)}(r,t)$, as in Fig. 8. Lines indicate the expected radial propagation calculated from the short branch of the linear Lin–Shu dispersion relation, for $\Omega_p = 10$–$50\,\mathrm{km\,s^{-1}\,kpc^{-1}}$, with $Q = 1$.

deeper and deeper structures are visible, down to about 10 arcsec. Partly the lack of structures with small N is the result of the rapid heating of the inner disc: for example, the run with the smallest N had $Q \approx 2$ inside $r = 50$ arcsec already after the initial 1 Gyr isolated period. On the other hand, for $N = 4 \times 10^6$, the heating was practically insignificant, despite of the moderately strong spiral structures which developed in the inner parts. Apparently the coherent spirals seen in large N runs are less effective in heating the innermost disc, as compared to random swing-amplified noise. This may be expected, since these spiral packets rotate with a nearly constant pattern speed near the centre and thus do not lead to increased velocity dispersion (see Binney & Tremaine 1987). Also, since they are able to travel through the centre, the dissipation of wave energy as a result of ILR is also absent.

Nevertheless, the lack of visible structures in Fig. 17 for small N is also related to the lack of necessary particle resolution. For example, the innermost discernable spiral segments in perturbed $N = 4 \times 10^6$ run are weakly present also for $N = 10^6$. With Fourier analysis, wave packets similar to those for $N = 4 \times 10^6$ can be identified even for $N = 2.5 \times 10^5$; also their shape can be deduced with the method applied in Fig. 9. Only in the run with $N = 60 \times 10^3$ are the central structures totally washed out by random noise.

3.5 Influence of Q and ϵ

A few additional experiments were performed with various values of Q. As may be expected, increased Q stabilizes the disc considerably both in isolated and in perturbed runs. For example, if Q was increased to 2, tidal arms could be followed only to about 60 arcsec for the standard perturbation strength and grid resolution. Also, we performed runs with different Q, ϵ_{grav} combinations, to check at least qualitatively the typically assumed correspondence between the velocity dispersion and softened gravity. Some examples are displayed in Fig. 16, showing essentially similar perturbed inner morphology as seen in the previous experiments. Especially, the shape of the spiral structure shows no apparent dependence on Q or ϵ_{grav}, supporting the generality of the k_{cr} dependence. For larger Q and ϵ_{grav} the inner disc stays fairly featureless, while reduced Q and ϵ_{grav} lead to unstable behaviour, already evident in the isolated evolution.

3.6 Live bulge

In the simulations presented so far, the major contribution to the force has been the result of the inert spherical component. Thus even large spiral perturbations seen in the inner disc surface density represent much milder perturbations in the total gravitational potential. This treatment should be justified, provided that the bulge is not significantly altered as a result of perturbation. In order to check this assumption, a single run with a live bulge was performed. In this experiment the bulge was represented by a Plummer sphere, with $M_{bulge} = 0.1 \times M_{disc}$ and with scale radius $R_{bulge} = 10$ arcsec. Combined with our exponential disc, this leads to a total surface density profile similar to the near-IR profile by Rix & Rieke (1993). The halo core radius was increased to

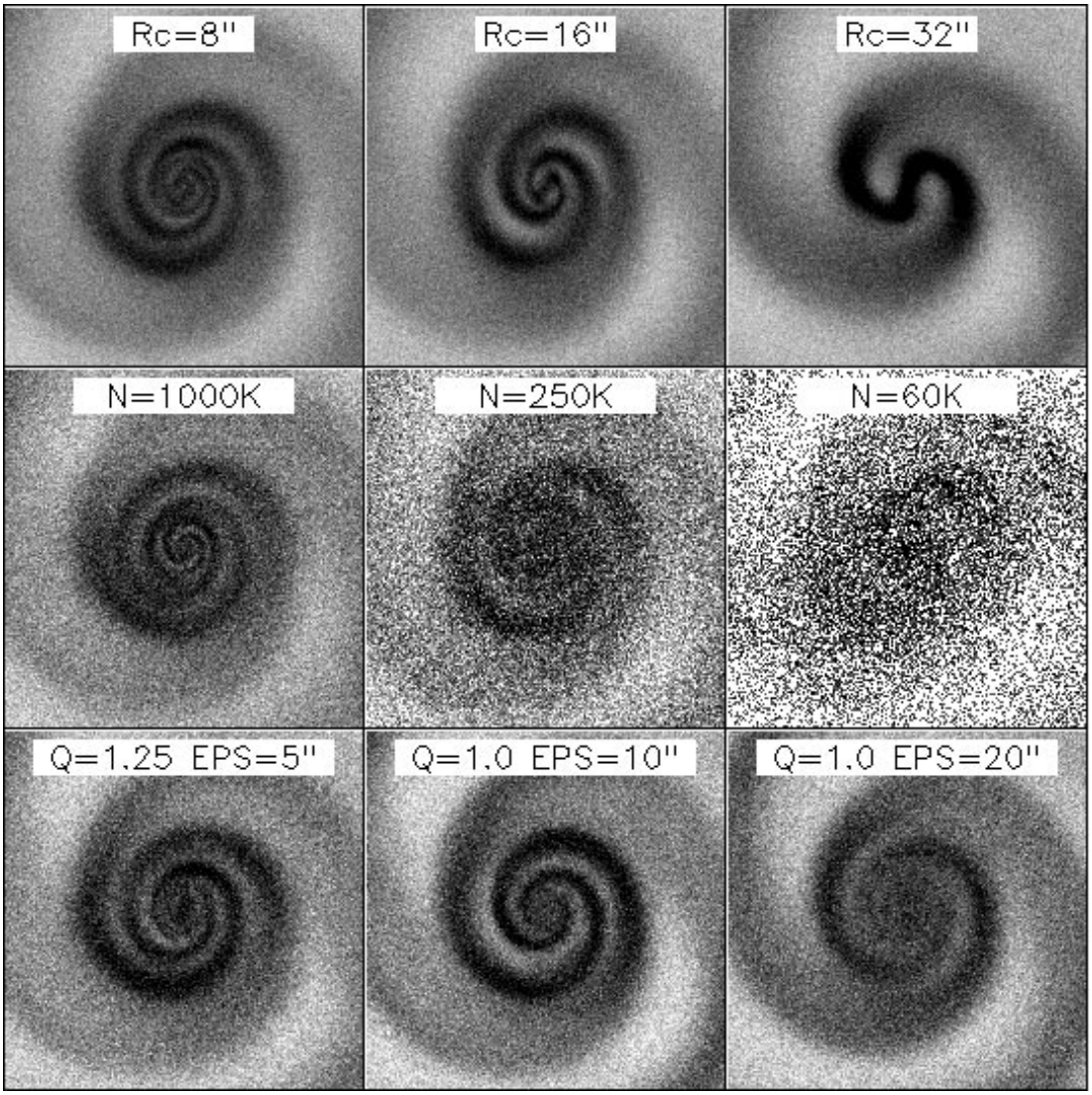

Figure 16. Uppermost row: influence of the slope of the inner rotation curve on the inner structure. Three different values of halo core radii, R_c, are studied, yielding a linearly rising inner portion of length of about $2R_c$. $N = 4 \times 10^6$. Middle row: comparison of runs with different number of particles. Lower row: different Q and ϵ_{grav} combinations in runs with $N = 10^6$. In each case the inner 200 by 200 arcsec region is displayed, for the standard perturbation at $T = 450$ Myr.

$R_c = 40$ arcsec and its mass was reduced to keep M_{tot} constant. This extended halo was still represented by a rigid potential, but its influence on the inner parts can be expected to be negligible. The positions and velocities for the bulge particles ($N_{bulge} = 10^5$) were created according to the phase-space distribution of a Plummer sphere (Binney & Tremaine 1987), without taking into account the disc or the halo. Since these contribute only little to the total potential in the bulge region, the bulge created in this manner is very near to equilibrium. The behaviour of this run was essentially similar to those with a rigid bulge.

3.7 Comparison with observations

An interesting feature of M51 is the amplitude variations seen along its spiral arms (Elmegreen et al. 1989). As already mentioned, this has been used as an argument to support the intrinsic origin of the spiral structure of M51 (Lin & Bertin 1995; Bertin & Lin 1996). However, there is no clear reason why such variations could not also develop during a prolonged tidal interaction. We have already seen how progressively larger frequencies are excited in the disc while the tidal wave propagates inward. The tidal wave thus behaves as a superposition of numerous wave packets, each attaining its largest amplitude near its ILR. An interference between these waves can be expected, as was seen in Fig. 14, where the normalized $m = 2$ amplitude had several local minima, and especially clearly in Fig. 15, displaying the separate waves associated with the propagation of the tidal perturbation. A more detailed comparison to observations is performed in Fig. 17, showing the $m = 2$ amplitude as a function of radius, both from near-IR observations [*Hubble Space Telescope* (*HST*) observations by Scoville & Evans (1998); Rix & Rieke 1993; Laurikainen et al., in preparation], and from the above simulation with a live bulge. Except for slight differences in the locations of the amplitude minima, the correspondence is evident.

The outermost observed minimum in $m = 2$ amplitude at

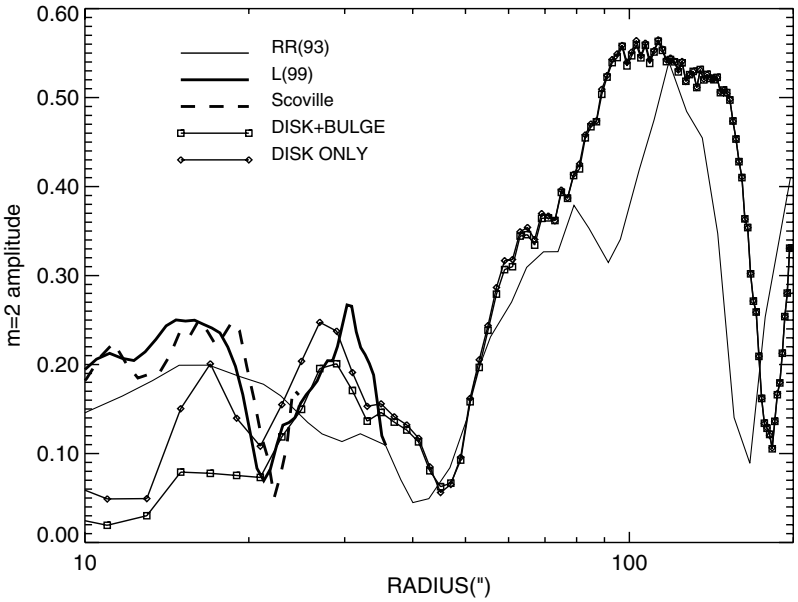

Figure 17. Comparison of the observed $m = 2$ amplitudes with the simulation with a live bulge and $M_d = 0.333$ exponential disc. Thin solid line stands for the *K*-band measurements of Rix & Rieke (1993), with 0.3 arcsec pixel size, thick solid lines denote the K'-band observations by Laurikainen et al. (in preparation), with 0.2 arcsec pixel size, and the dashed line is measured from the *HST* image by Scoville & Evans (1998) (Nicmos 2 camera with F222M filter): we made a crude calibration by normalizing the $m = 0$ profile of the *HST* image to Rix & Rieke (1993) observations. Lines with symbols stand for $m = 2$ components derived from the simulation at the nominal observing time $T = 450$ Myr, with and without inclusion of the bulge particles.

$\approx$180 arcsec is related to the change in the curvature of the arms. In the simulations a similar feature is seen, and it appears to be related to a distance where the main spiral structure, as a result of its self-gravity, shows a tendency to separate from the kinematically evolving outer tidal structures. This interpretation is supported also by Fig. 14, indicating how the minimum in $m = 2$ amplitude at $r \approx 200$ arcsec, around $T = 400$ Myr, gets more pronounced when the disc mass is increased. This feature is also visible in the single encounter model, indicating that the second crossing, although it can in principle affect the shape of the outer arms, is not responsible for the minimum. The minima at $r \approx 40$ and $\approx$20 arcsec seem to be more genuine amplitude variations, in the sense that they are related to the strength of the spiral, not to its shape. In simulations these features are related to the interference of separate tidal packets. The close correspondence in their positions in Fig. 17 with observations is partly fortuitious, as the locations of these minima depend on time. The observed amplitudes of about 0.2 inside $r = 20$ arcsec correspond to the central oval, which is rather weak in the studied $M_d = 0.333$ simulation.

Another comparison is shown in Fig. 18, displaying examples of the simulated inner structures together with the HST narrow *K*-band observations made by Scoville & Evans (1998). The frame in the upper left displays the *K*-image after subtraction of the $m = 0$ component, while in the lower left, a smoothed image has been subtracted, enhancing the contrast of the inner trailing spirals, first discovered by Zaritsky et al. (1993). Interestingly, the upper *HST* image gives an impression of open leading spirals inside the central bar. There is a striking similarity between this leading structure and the occasional leading morphology seen in the simulations, which resulted from the reflection of strong leading packets from the centre, and their interference with the trailing waves. The time-step of the simulation example in the upper right, for $M_d = 0.5$, has been deliberately chosen to represent such structures. The lower simulation frame in the right is for $M_d = 0.333$, and corresponds to the nominal observing time. Except for the central oval, the resemblance to observed morphology is good. Note that in both simulations a single exponential profile has been used to describe the distribution of the active disc mass. An increase of the active disc mass inside about 15 arcsec, with respect to the $M_d = 0.333$ exponential profile, might well produce a combination of the two simulation snapshots, yielding simultaneously a stronger oval and tightly wound spirals.

4 DISCUSSION

We have made an attempt to study the inner structure of M51 with simulation models, in which the initial disc profile is assumed to obey a single exponential profile, and in which the combined rotation curve arising from a live disc and an analytical halo matches the observed inner slope. Two different models for the relative contribution of the disc and halo have been systematically explored ($M_d = 0.333$ and 0.5), while experiments with different halo core radii ($R_c = 8$–32 arcsec) highlighted the importance of the inner rotation curve. Experiments with various *N* and different amount of softening have been conducted, in order to check the influence of simulation-method related parameters. Moreover, a single experiment with a live bulge was performed, to justify our use of rigid halo potential. In addition to simulations with a tidal perturbation, the properties of our model when evolved in isolation have been studied in considerable detail. The tidal perturbation has been chosen such that it is able to reproduce the large-scale morphological and kinematical observations (see Paper I).

Our simulation disc, when evolved in isolation, corresponds to a typical late-type spiral with multi-armed outer structure. As a result of large *N* employed in simulations, the evolution of the velocity dispersion of the disc is fairly low, and the spiral

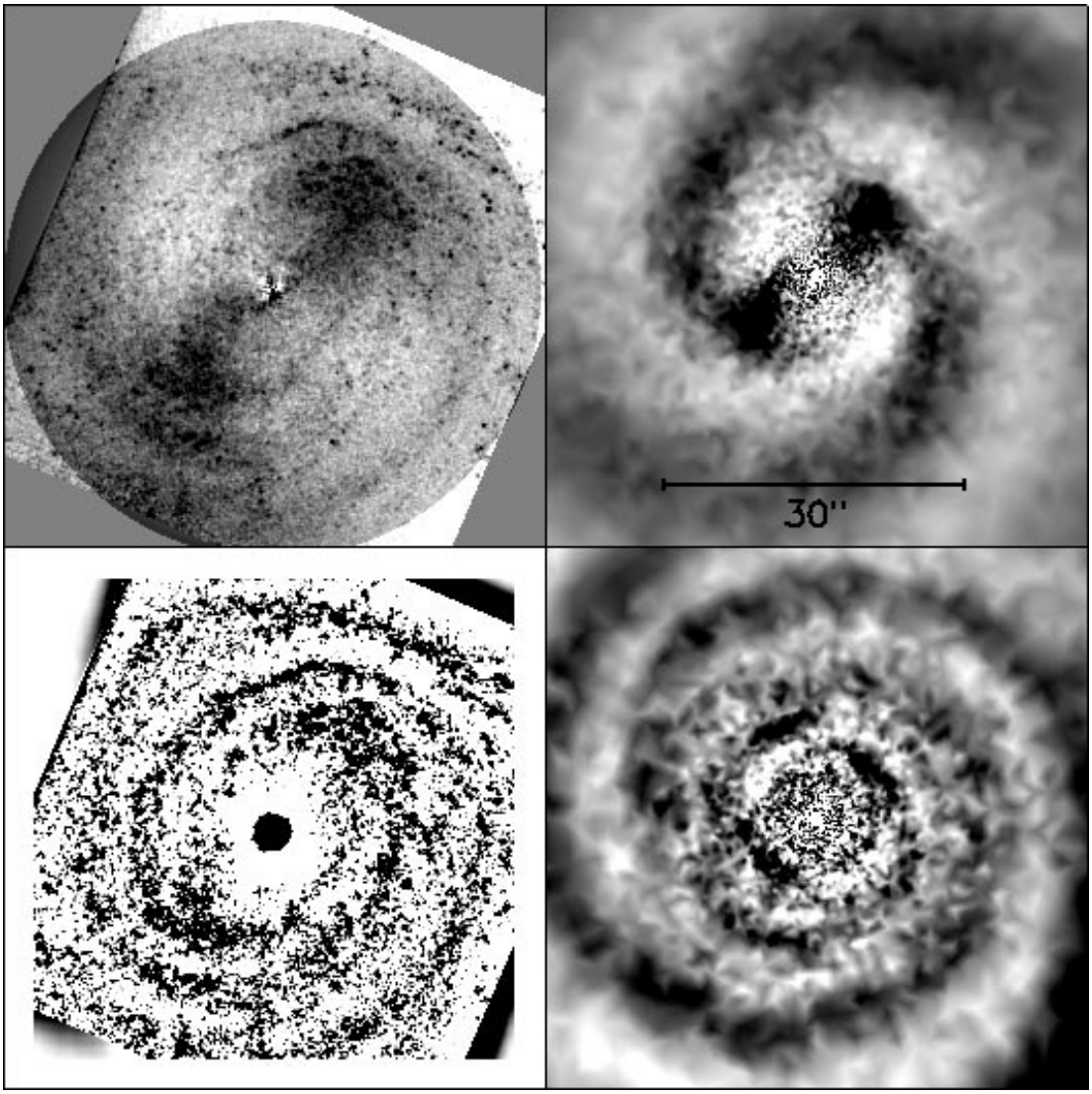

Figure 18. Comparison with *HST* observations by Scoville & Evans (1998) (Nicmos 2 camera with F222M filter). In the upper left the *HST* image after subtraction of the $m = 0$ component is shown, while in the lower left a 20-pixel-wide boxcar average has been subtracted. The simulation in the upper right corresponds to $M_{\rm d} = 0.5$, while on the lower right $M_{\rm d} = 0.333$.

structures exhibit practically no secular changes during the about 3-Gyr span of simulations. The inner parts of the disc are fairly reactive, dominated with continuously re-emerging $m = 2$ spiral patterns. With the good resolution of the central regions, even the reflection of some individual trailing packets as leading waves from the centre was discerned. These waves had such a high pattern speed that they did not possess any ILR. Interestingly, the shape of individual waves does not follow the linear Lin–Shu dispersion relation, nor are they able to maintain their pattern speeds at a constant level. However, the radial propagation of amplitudes is comparable to the group velocity calculated from the Lin–Shu relation, using similar pattern speeds. Within the steeply rising inner part of the rotation curve, where $\lambda_{\rm cr}/r$ is large, the waves tend to have an oval shape. Thus, even in isolation the innermost disc ($r < 30$ arcsec) developed structures which in many instances resemble the tightly-wound central spirals of M51. However, these $m = 2$ spirals lack continuity with the weaker outer structures with higher m. The origin of these spirals was not addressed in any detail, but a likely explanation might be the type of recurrent instabilities studied by Sellwood and his co-workers (e.g. Sellwood & Lin 1989; Sellwood & Kahn 1991).

During a tidal perturbation by a fairly massive companion, prominent $m = 2$ waves supersede all outer structures and by the nominal observing time ($T = 450$ Myr) extend well inside 30 arcsec. Toomre has presented two different scenarios for the formation of tidal spirals. According to his original view (Toomre 1969), the tidal distortions of the outer disc evolve into propagating wave packets, which travel inward with the group velocity. Later Toomre (1981) discarded this scenario, at least for M51, as the implied propagation time exceeded the $\sim$100 Myr duration of his original single passage model (Toomre & Toomre 1972). Instead he proposed that the *in situ* swing amplification of weak kinematic disturbances could lead to a strong response in the inner disc. As the time-scale of the swing amplification cycle is proportional to the local orbital period, inner spirals could develop even more rapidly than the outer ones. This has later been accepted as a standard tidal explanation for the spiral structure of M51 (see e.g. Combes et al. 1995).

However, the time evolution of $m = 2$ amplitudes in our simulations gives support to Toomre's original radial propagation model: after rapid excitation of the disc at $r > 100$ arcsec, the $m = 2$ density amplitudes were seen to evolve from the outer disc toward the interior, with speeds compatible with the characteristic group velocity. As the propagation in our model was initiated about 500 Myr ago, there is no time-scale problem in the current simulations. On the other hand, the *in situ* amplification also occurs, but mainly in the outer disc, as the low angular velocity of the direct excitation places its ILR at the outer disc ($r >$ 100 arcsec). The signature of this type of excitation might be the above-mentioned almost simultaneous emergence of increased $m = 2$ amplitudes outside $r = 100$–200 arcsec, seen in Fig. 14. These are much stronger than the purely kinematical response which is obtained in the same radial range in simulations with zero disc mass. To further check the role of *in situ* swing amplification, we also experimented with models in which the perturber was replaced by an artificial forcing, with constant pattern speeds corresponding to well-defined ILRs at much deeper regions, at $r = 30$–60 arcsec. In these cases the response was indeed strongest much deeper in the disc, near the implied ILRs, in agreement with the similar models by Toomre (1981). Also the deformation of the outer disc was rather weak in the experiments with fast forcing (say, $\Omega_p = 40\,\mathrm{km\,s^{-1}\,kpc^{-1}}$), and could not initiate any significant radial inward propagation.

The azimuthal speed of the tidal wave increases during its inward propagation, exciting frequencies near $\Omega - \kappa/2$ at each distance. However, this resemblance to kinematic waves is probably just superficial, the wave representing rather a superposition of several packets, attaining largest amplitudes near their ILRs. Amplitude variations along the spiral arms, resembling at least qualitatively those seen in observations, arose naturally in the simulations when the tidal wave had propagated deep into the disc. The presence of amplitude variations does thus not rule out tidal origin of spiral arms, being rather an indication of the advanced age of the perturbation.

The eventual fate of the inward propagating tidal wave depended on the strength of the perturbation, and the reactivity of the disc, the latter affecting also the strength of the intrinsically formed inner structures. For example, a tidal perturbation with half as massive a companion as with our nominal value of $M_p = 0.55$ was able to excite a tidal wave that penetrated only to about 50–60 arcsec, at least during the time-span of the simulation. The same was true for a less massive disc with $M_d = 0.2$. With the nominal values for M_p and M_d, the wave could be followed even to 10 arcsec, if there were no strong pre-existing inner waves. If these were present, the behaviour was determined by the interplay of intrinsic and tidal waves. However, as the azimuthal speed of the tidal wave at each distance seems to be comparable to the pattern speed of the intrinsic waves, the typical result of this interplay was at many instants of time a smooth joining of the patterns. Also, in other cases the tidal excitation was able to excite modes which, although clearly present, had remained very weak in the isolated case. This was clear in the cases where the extent of the linearly rising rotation curve was increased, lowering the $\Omega - \kappa/2$ barrier, and the perturbation excited the formation of a central bar.

In Paper I we showed that the simulated current morphology (at least beyond about 50 arcsec) can remain practically unaltered, even if the previous disc-plane crossings implied by the bound model are taken into account. This is possible provided that the previous crossing distances have been at least about 30 per cent larger than the southern crossing, implying a perturbation strength less than about one half of the most current perturbation. Thus it is likely that the outer disc deformations during previous passages have been so weak that inward propagating tidal packets have been not able to reach the innermost 30-arcsec region.

The overall picture presented by the current simulations deviates significantly from the previous studies, in which single modes with fixed pattern speeds have been assumed for the spiral structure of M51. The deduced values of pattern speeds in various studies were shown in Fig. 13. The fits by Tully (1974b) and Shu et al. (1971) applied the linear Lin–Shu dispersion relation, while in the study of Garcia-Burillo, Guélin & Cernicharo (1993) the pattern speed was determined from simulations in which the morphology of colliding test particles was followed in rigidly rotating spiral potentials with different values of Ω_p. The pattern speed estimates range between 20 and $40\,\mathrm{km\,s^{-1}\,kpc^{-1}}$, and thus correspond roughly to the intermediate range of frequencies seen in the current models for 30–150 arcsec. This is also the region in which the single wave fits gave quite a good match for the observed morphology. In Elmegreen, Elmegreen & Seiden (1989) it was proposed that two pattern speeds are required for the structure of M51 beyond $r > 30$ arcsec, the inner mode corresponding to Tully's (1974b) fit, with corotation at $r \approx 130$ arcsec, and an outer mode describing the optical bridge and tail region. They further proposed that the patterns would be connected by a non-linear mode-coupling (Tagger et al. 1987), so that the ILR of the outer mode would coincide with the corotation distance of the inner one. Nevertheless, the current tidal model accounts naturally for the outer morphologies.

Interestingly, in our tidal models we also have two dominant ranges of frequencies, which at first glance fall close to CR–ILR coupling: in the innermost disc we have $\Omega_p \sim 50\,\mathrm{km\,s^{-1}\,kpc^{-1}}$, with CR (corotation resonance) at about 100 arcsec, which is also near the typical ILR distance of the outer strong frequencies around 10–$20\,\mathrm{km\,s^{-1}\,kpc^{-1}}$ (see Fig. 13). However, in the current models this relation between the prominent inner and outer frequencies is largely coincidental: the inner waves have pattern speeds which are just above the $\Omega - \kappa/2$ maximum, while the outer frequencies are determined mainly by the external forcing, and the lowest pattern speeds sustained by the disc. For example, in the simulations performed with larger values of R_c the outer frequencies were practically identical to those above, whereas the inner disc frequencies were lower, in accordance with the reduced $\Omega - \kappa/2$ maximum: in this case there was no possibility of making any identifications in support of mode coupling. Also, there is hardly enough time to establish any actual mode-coupling, as a result of the transient nature of the evolution. Indeed, the mode-coupling (Masset & Tagger 1997) seems reasonable only between strong long-lived modes, e.g. between large-scale bars and outer spirals (see Rautiainen & Salo 1999).

5 CONCLUSIONS

A survey of numerical simulations has been conducted for the M51 system, performed with a large number of particles (up to $N = 4 \times 10^6$), and a good gravity resolution. The models were based on the velocity curve and radial mass distributions consistent with observations, and the assumed mass ratio for the galaxies, 0.55, seems fairly reasonable. Note that the same models can explain the morphology of the innermost regions at $r <$ 30 arcsec and the optical spiral arms, as well as the extended H I

tail observed by Rots et al. (1990), including its apparent velocity field reversal as compared to the central disc (see Paper I). The nominal parameters for the disc of M51 were $Q = 1.5$ and disc-to-total-mass ratio $M_{\rm d} = 0.333$ for $r < 400$ arcsec, assuring its large-scale stability. Based on these simulations, the following conclusions can be drawn.

(1) The current spiral structure of M51 can be accounted for by a prolonged tidal perturbation, including the innermost oval/spiral structure inside 30 arcsec, discovered in near-IR by Zaritsky et al. (1993). The requirements for the M51-type innermost structure are quite stringent: long and strong enough perturbation (duration of the order of 5×10^8 yr, companion mass ratio $\approx$0.5), moderately massive disc ($M_{\rm d} \approx 0.333$), and cool enough inner regions ($Q_{\rm eff} \approx 2$). Also, the rotation curve must have a steep inner slope and thus large maximum value of $\Omega - \kappa/2$ to protect the disc against the formation of a large-scale bar during the perturbation.

(2) The main mechanism responsible for the deeply penetrating spiral arms inside 100 arcsec is the tidal wave induced by the direct perturbation of the outer disc, the perturbation amplitudes progressing inward with speeds comparable to the estimated group velocity, as proposed in Toomre (1969, 1977). Any strong excitation by the *in situ* swing amplification (Toomre 1981) is likely to be limited outside about 100 arcsec, because of the low frequency of the direct forcing. The tidal spirals cannot be characterized by a single pattern speed, as higher and higher frequencies are excited when the wave proceeds inward, with maximum amplitudes occurring near the $\Omega - \kappa/2$ curve.

(3) Amplitude variations along spiral arms arise naturally during the propagation of the wave, as a result of the interference of separate tidal packets.

(4) The innermost regions of the studied disc model exhibit recurrent $m = 2$ spiral patterns also in the absence of perturbations. Their shape follows fairly accurately the empirical $k_{\rm cr}$ relation, previously found by Donner & Thomasson (1994), while their radial propagation speeds are comparable to the group velocity calculated from the linear Lin–Shu dispersion relation. These inner packets show no signs of decay during the about 3-Gyr time-span of our simulations. Individual strong waves lacking ILR can reflect from the centre as leading ones, strong enough to be visible in direct density plots. This might bear relevance for the leading central structures seen in M51 and in some other galaxies in the recent *HST* observations (e.g. Knapen et al. 1995).

(5) The innermost spiral structure represents an interplay between the intrinsic central spirals and the inward propagating tidal wave. As the shapes and pattern speeds of the waves are fairly similar regardless of their origin, this interplay can lead to a smooth continuation of the arms, as seen in observations.

In general, the evolution in isolation and during the perturbation show many similarities. For example, $m = 2$ waves with similar pattern speeds are seen, and the shapes of these patterns resemble each other. This is clearly in accordance with the view by Lin & Bertin (1995), according to which tidal perturbations excite behaviour which is already latent in the isolated case. Nevertheless, according to our M51 models, the role of perturbation cannot be considered secondary, as the external excitation alone seems to be able to account for practically all of the structure beyond 30 arcsec, and also to be responsible for the continuity of the structure even inside 30 arcsec.

ACKNOWLEDGMENTS

We thank the referee, Dr J. Dubinski, for his useful suggestions. This study has utilized observations made with the NASA/ESA *Hubble Space Telescope*, obtained from the data archive at the Space Telescope Science Institute. STScI is operated by the Association of Universities for Research in Astronomy, Inc. under NASA contract NAS 5-26555. The support from the Academy of Finland is acknowledged.

REFERENCES

Binney J., Tremaine S., 1987, Galactic Dynamics. Princeton Univ. Press, Princeton
Bertin G., Lin C. C., 1996, Spiral Structure in Galaxies. MIT Press, Cambridge, MA
Bertin G., Lau Y. Y., Lin C. C., Mark J. W. K., Sugiyama L., 1977, Proc. Nat. Acad. Sci., 74, 4726
Combes F., Boisse P., Mazure A., Blanchard A., 1995, Galaxies and Cosmology. Springer, Heidelberg
Donner K. J., Thomasson M., 1994, A&A, 290, 785
Elmegreen B. G., Elmegreen D. M., Seiden P. E., 1989, ApJ, 343, 602
García-Burillo S., Guélin M., Cernicharo J., 1993, A&A, 274, 148
Hernquist L., 1990, in Wielen R., ed., Dynamics and Interactions of Galaxies. Springer, Heidelberg, p. 108
Julian W. H., Toomre A., 1966, ApJ, 146, 810
Knapen J. H., Beckman J. E., Schlosman I., Peletier R. F., Heller C. H., De Jong R. S., 1995, ApJ, 443, L73
Lin C. C., Bertin G., 1995, Ann. New York Acad. Sci., 773, 125
Lin C. C., Shu F. H., 1964, ApJ, 140, 646
Lowe S. A., Roberts W. W., Yang J., Bertin G., Lin C. C., 1994, ApJ, 427, 184
Masset F., Tagger M., 1997, A&A, 322, 442
Miller R. H., 1971, Ap&S, 14, 73
Noguchi M., 1987, MNRAS, 228, 635
Noguchi M., 1996, ApJ, 469, 605
Rand R. J., 1993, ApJ, 410, 68
Rautiainen P., Salo H., 1999, A&A, 348, 737
Rix H.-W., Rieke M. J., 1993, ApJ, 418, 123
Romeo A. B., 1994, A&A, 286, 799
Rots A. H., Bosma A., van der Hulst J. M., Athanassoula E., Crane P. C., 1990, AJ, 100, 387
Salo H., 1991, A&A, 243, 118
Salo H., Laurikainen E., 1993, ApJ, 410, 586
Salo H., Laurikainen E., 2000, MNRAS, 319, 377 (Paper I, this issue)
Scoville N., Evans A., 1998, Space Telescope Science Institute data archive
Sellwood J. A., Carlberg R. G., 1984, ApJ, 282, 61
Sellwood J. A., Kahn F. D., 1991, MNRAS, 250, 278
Sellwood J. A., Lin D. N. C., 1989, MNRAS, 240, 991
Shu F. H., Stachnik R. V., Yost J. C., 1971, ApJ, 166, 465
Spitzer L., 1942, ApJ, 95, 329
Tagger M., Sygnet J. F., Athanassoula E., Pellat R., 1987, ApJ, 318, L43
Thomasson M., Donner K. J., Elmegreen B. G., 1991, A&A, 250, 316
Tilanus R. P. J., Allen R. J., 1991, A&A, 244, 8
Toomre A., 1964, ApJ, 139, 1217
Toomre A., 1969, ApJ, 158, 899
Toomre A., 1977, ARA&A, 15, 437
Toomre A., 1981, in Fall S. M., Lynden-Bell D., eds, The Structure and Evolution of Normal Galaxies. Cambridge Univ. Press, Cambridge, p. 111
Toomre A., Toomre J., 1972, ApJ, 178, 623
Tully R. B., 1974a, ApJS, 27, 437
Tully R. B., 1974b, ApJS, 27, 449
White R. L., 1988, ApJ, 330, 26
Zang T. A., 1976, PhD thesis, Massachusetts Inst. of Technology, Cambridge, MA
Zaritsky D., Rix H.-W., Rieke M., 1993, Nat, 364, 313

This paper has been typeset from a TEX/LATEX file prepared by the author.